

The Open University's repository of research publications  
and other research outputs

## Trajectory estimation for particles observed in the vicinity of (101955) Benu

### Journal Item

#### How to cite:

Chesley, S. R.; French, A. S.; Davis, A. B.; Jacobson, R. A.; Brozović, M.; Farnocchia, D.; Selznick, S.; Liounis, A. J.; Hergenrother, C. W.; Moreau, M. C.; Pelgrift, J.; LessacChenen, E.; Molaro, J. L.; Park, R. S.; Rozitis, B.; Scheeres, D. J.; Takahashi, Y.; Vokrouhlický, D.; Wolner, C. W. V.; Adam, C.; Bos, B. J.; Christensen, E. J.; Emery, J. P.; Leonard, J. M.; McMahon, J. W.; Nolan, M. C.; Shelly, F. C. and Laretta, D. S. (2020). Trajectory estimation for particles observed in the vicinity of (101955) Benu. *Journal of Geophysical Research: Planets (Early Access)*.

For guidance on citations see [FAQs](#).

© 2020 American Geophysical Union

Version: Accepted Manuscript

Link(s) to article on publisher's website:  
<http://dx.doi.org/doi:10.1029/2019je006363>

---

Copyright and Moral Rights for the articles on this site are retained by the individual authors and/or other copyright owners. For more information on Open Research Online's data [policy](#) on reuse of materials please consult the policies page.

---

1 **Trajectory estimation for particles observed in the**  
2 **vicinity of (101955) Bennu**

3 **S. R. Chesley<sup>1</sup>, A. S. French<sup>2</sup>, A. B. Davis<sup>2</sup>, R. A. Jacobson<sup>1</sup>, M. Brozović<sup>1</sup>,**  
4 **D. Farnocchia<sup>1</sup>, S. Selznick<sup>3</sup>, A. J. Liounis<sup>4</sup>, C. W. Hergenrother<sup>3</sup>, M. C.**  
5 **Moreau<sup>4</sup>, J. Pelgrift<sup>5</sup>, E. Lessac-Chenen<sup>5</sup>, J. L. Molaro<sup>8</sup>, R. S. Park<sup>1</sup>, B.**  
6 **Rozitis<sup>6</sup>, D. J. Scheeres<sup>2</sup>, Y. Takahashi<sup>1</sup>, D. Vokrouhlický<sup>7</sup>, C. W. V. Wolner<sup>3</sup>,**  
7 **C. Adam<sup>5</sup>, B. J. Bos<sup>4</sup>, E. J. Christensen<sup>3</sup>, J. P. Emery<sup>9</sup>, J. M. Leonard<sup>2</sup>, J. W.**  
8 **McMahon<sup>2</sup>, M. C. Nolan<sup>3</sup>, F. C. Shelly<sup>3</sup>, D. S. Lauretta<sup>3</sup>**

9 <sup>1</sup>Jet Propulsion Laboratory, California Institute of Technology, Pasadena, California, USA

10 <sup>2</sup>University of Colorado, Boulder, Colorado, USA

11 <sup>3</sup>Lunar and Planetary Laboratory, University of Arizona, Tucson, Arizona, USA

12 <sup>4</sup>Goddard Space Flight Center, Greenbelt, Maryland, USA

13 <sup>5</sup>KinetX Aerospace, Simi Valley, California, USA

14 <sup>6</sup>The Open University, Milton Keynes, UK

15 <sup>7</sup>Institute of Astronomy, Charles University, Prague, Czech Republic

16 <sup>8</sup>Planetary Science Institute, Tucson, Arizona, USA.

17 <sup>9</sup>Northern Arizona University, Flagstaff, Arizona, USA

18 **Key Points:**

- 19 • Most of the 313 particles we study have sub-orbital trajectories but some orbit Bennu  
20 and others directly escape  
21 • The particles appear to have flake-like shapes and have effective diameters 0.22–  
22 6.1 cm with median 0.74 cm  
23 • Ejections tend to take place in the local afternoon and evening but can occur any-  
24 time

---

Corresponding author: Steven Chesley, [steve.chesley@jpl.nasa.gov](mailto:steve.chesley@jpl.nasa.gov)

This article has been accepted for publication and undergone full peer review but has not been through the copyediting, typesetting, pagination and proofreading process which may lead to differences between this version and the Version of Record. Please cite this article as doi: 10.1029/2020JF005411

## Abstract

We analyze the trajectories of 313 particles seen in the near-Bennu environment between December 2018 and September 2019. Of these, 65% follow sub-orbital trajectories, 20% undergo more than one orbital revolution around the asteroid, and 15% directly escape on hyperbolic trajectories. The median lifetime of these particles is  $\sim 6$  h. The trajectories are sensitive to Bennu’s gravitational field, which allows us to reliably estimate the spherical harmonic coefficients through degree 8 and to resolve nonuniform mass distribution through degree 3. The particles are perturbed by solar radiation pressure, enabling effective area-to-mass ratios to be estimated. By assuming that particles are oblate ellipsoids of revolution, and incorporating photometric measurements, we find a median axis ratio of 0.27 and diameters for equivalent-volume spheres ranging from 0.22–6.1 cm, with median 0.74 cm. Our size distribution agrees well with that predicted for fragmentation due to diurnal thermal cycling. Detailed models of known accelerations do not produce a match to the observed trajectories, so we also estimate empirical accelerations. These accelerations appear to be related to mismodeling of radiation pressure, but we cannot rule out contributions from mass loss. Most ejections take place at local solar times in the afternoon and evening (12:00–24:00), although they occur at any time of day. We independently identify ten ejection events, some of which have previously been reported. We document a case where a particle ricocheted off the surface, revealing a coefficient of restitution  $0.57 \pm 0.01$  and demonstrating that some apparent ejections are not related to surface processes.

## Plain Language Summary

The OSIRIS-REx mission discovered that near-Earth asteroid (101955) Bennu is periodically ejecting small particles from its surface, placing it in the uncommon class of “active asteroids”. We linked together individual detections of ejected particles and used numerical models of the forces acting on them to ascertain their trajectories and fates. We found that most particles have sub-orbital trajectories, meaning they fall back to Bennu’s surface shortly after being ejected, but some orbit Bennu for days at a time, and some escape directly into space. From the particle trajectories, we are able to estimate their sizes (comparable to pebbles, from a few millimeters to a few centimeters in diameter) and shapes (probably flake-like). Their trajectories also make it possible to estimate Bennu’s gravity field more precisely than spacecraft measurements and help shed light on the possible causes of the ejections.

## 1 Introduction

One of the early surprises for NASA’s OSIRIS-REx asteroid sample return mission occurred shortly after the spacecraft entered into orbit around its target, the near-Earth asteroid (101955) Bennu. OSIRIS-REx navigational images from 6 January 2019 revealed that particles were being ejected from the asteroid surface into the spacecraft environs (Hergenrother et al., 2019). The particles were small, initially estimated to be roughly 1–10 cm in diameter, and the velocities were relatively low, up to a few meters per second, thus the immediate concerns about spacecraft safety were quickly allayed (Lauretta et al., 2019). However, these particle detections raised questions. For example, what is causing the particle ejections? What are the physical properties of the particles, such as mass, size, shape, and albedo? What are the ejection circumstances, such as velocity and time of day? What is the frequency of ejection events? Our paper builds on the work of Lauretta et al. (2019) by computing the trajectories of hundreds of ejected particles detected between December 2018 and September 2019. This longer time frame and greater number of analyzed particles allows us to make further inferences and draw conclusions about the particle dynamics in Bennu’s environment and, in turn, to add constraints to the nature of the ejection mechanism.

75 The discovery of small particles leaving its surface puts Bennu in the category of  
76 active asteroids. Until recent decades, comets were distinguished from asteroids primar-  
77 ily by the presence of observable activity, with asteroids being generally presumed as in-  
78 ert bodies. The discovery of so-called main-belt comets represented a fundamental shift  
79 in the way asteroids are conceived. We now have many asteroids—in both the main belt  
80 and near-Earth populations—that appear to be active, and there are several disparate  
81 mechanisms that appear to be causing the activity. Sublimation of volatiles appears as  
82 a likely explanation for many (Hsieh & Jewitt, 2006), while ejecta from small impactors  
83 has been proposed for others, and these two phenomena could work hand in hand, with  
84 small impactors exposing buried ices, leading to sustained activity after the impact ejecta  
85 have dispersed (Jewitt et al., 2015). Other cases appear to be driven by rotational fis-  
86 sion, with rapid rotators episodically shedding material (Jewitt et al., 2013). The pos-  
87 sibility that thermal cycling could lead to sudden fracturing and energetic release of frag-  
88 ments has been studied in the laboratory (Delbo et al., 2014) and has been proposed for  
89 the activity seen from (3200) Phaethon at small heliocentric distance (Li & Jewitt, 2013)  
90 and to explain the apparent paucity of small, dark asteroids at low perihelion distances  
91 (Granvik et al., 2016).

92 In the context of Bennu’s activity, multiple mechanisms have recently been stud-  
93 ied. Hartzell et al. (2019 in review, this collection) explore the possibility of particle loft-  
94 ing due to electrostatic charging of particulates and find this to be an unlikely explana-  
95 tion for Bennu’s activity, although it cannot be ruled out for small nightside ejection events.  
96 From high-resolution thermal modeling, Rozitis et al. (2019 in review, this collection)  
97 conclude that ice sublimation is not a plausible explanation but that high diurnal tem-  
98 perature amplitudes create conditions favorable to thermal fracturing. Molaro et al. (2019  
99 in review, this collection) test thermal fracturing models, finding that thermal fractur-  
100 ing should lead to exfoliation on Bennu and could eject centimeter-scale particles at speeds  
101 up to meters per second, consistent with Bennu’s observed activity (Lauretta et al., 2019).  
102 Bottke et al. (2019 in review, this collection) examine the hypervelocity meteoroid flux  
103 at Bennu and report that such impacts could readily explain the evident energy and fre-  
104 quency of particle ejection events, predicting—like Molaro et al. (2019 in review, this collection)—  
105 that most such ejections should occur in the afternoon and evening, local solar time on  
106 Bennu. Both the meteoroid and thermal fracturing models predict increased activity at  
107 lower heliocentric distances, i.e., at perihelion.

108 We present a catalog of particle trajectories that is based on dedicated and serendip-  
109 itous tracking of their positions and that is affected by significant selection effects. While  
110 Bennu’s Hill sphere extends to 31 km (Rieger et al., 2019), our detections are from a nearby  
111 spacecraft with its camera oriented towards Bennu, thus our particles occupy only a small  
112 fraction of the Hill sphere. Also, we require at least three detections to obtain an orbital  
113 solution, which eliminates the possibility of obtaining orbits of objects that rapidly leave  
114 Bennu’s vicinity or are only lofted for a brief period. Finally, there is a lower size limit  
115 beyond which the particles are too small to allow sufficient signal in the images. Taken  
116 together, these limitations imply that we have only those particles that are large enough  
117 and remain in flight and near Bennu for long enough to estimate the trajectory. Another  
118 important consideration is that, over the nine months for which we have data, the ca-  
119 dence of particle tracking images varied greatly, which has a profound effect on our abil-  
120 ity to link detections to discern particle trajectories. The exact nature and effect of these  
121 selection effects remains as work to be done, but with the trajectories presented here,  
122 we can already see a portrait of the rich dynamical environment that these particles in-  
123 habit.

124 The dynamics of particles in orbit about a small body and strongly perturbed by  
125 solar radiation pressure (SRP) has been studied over the past decades for both cometary  
126 and asteroidal bodies. For comets, the impetus is to study the dynamics of lofted par-  
127 ticles that are large enough to remain bound to the nucleus. To do this, Richter and Keller

128 (1995) developed an analysis looking at the dynamics of the particles using angular mo-  
129 mentum and the eccentricity vectors as independent variables. Independently, Mignard  
130 and Henon (1984) showed that this basic problem was integrable when averaged and worked  
131 out the details of that solution for a body in a circular orbit about the Sun. In a later  
132 series of papers, Scheeres and co-workers combined and generalized these studies, show-  
133 ing that the integrable solution extends to the case when the small body is in an ellip-  
134 tic orbit about the Sun and can be generalized to a non-cannonball model (Scheeres, 1999,  
135 2012b; Rosengren & Scheeres, 2014). Contemporaneous with these studies was work by  
136 Dankowicz (1994, 1995), and later Scheeres and Marzari (2002), that developed condi-  
137 tions for particle capture when subject to SRP. When combined, these models provide  
138 an accurate representation of motion about a small body when strongly perturbed by  
139 SRP. A main application of these studies is to spacecraft dynamics about asteroids and  
140 comets (Scheeres, 2012a), and the OSIRIS-REx mission uses this theory for the design  
141 of its stable terminator orbits.

142 The hallmarks of motion of a particle in orbit about a small body and perturbed  
143 by SRP can be fully understood by combining these analyses. When bound, the motion  
144 in terms of orbit elements will be periodic, with a period less than one asteroid year, and  
145 with the period decreasing with increasing SRP perturbation strength. Thus, a parti-  
146 cle ejected from the surface of an asteroid will tend to come back to the surface again,  
147 after a period of time, as the initial ejection orbit elements will repeat. Still, the time  
148 between ejection and this return can be on the order of days to weeks and months, de-  
149 pending on the SRP strength and ejection conditions. For particles that move far from  
150 the small body, yet are still bound, their motion can closely mimic the ideal SRP solu-  
151 tions. For particles ejected at lower speeds and which remain closer to the asteroid, the  
152 effect of the asteroid oblateness and higher-order gravity field coefficients can have as large  
153 an effect as the SRP perturbations and create motion that is more chaotic in general (Scheeres,  
154 2012b). However, as we show in Sec. 5.6, such interactions also create an opportunity  
155 as they can provide insight into the mass distribution of the asteroid.

156 Our work dovetails with that of McMahon et al. (2019 in review, this collection),  
157 who generated a large number of synthetic trajectories in the Bennu environment, sys-  
158 tematically covering the range of particle ejection locations and circumstances. Their work  
159 provides a useful touchstone for the broad range of possible particle dynamics near Bennu,  
160 while our work documents what is actually seen. Taken together these approaches rep-  
161 resent a pathway to eventual debiasing of the observed particle population.

162 In the following sections, we describe our observational data (Sec. 2), and then pro-  
163 vide the details of our dynamical model (Sec. 3) and the orbit fitting process (Sec. 4).  
164 This is followed by a description and discussion of the various results (Sec. 5). We close  
165 with a listing of key conclusions.

## 166 **2 Observational Data**

167 The observational data for this effort are from a catalog of transient detections seen  
168 in images taken by the OSIRIS-REx NavCam 1 imager, part of the Touch and Go Cam-  
169 era System (TAGCAMS) (Bos et al., 2018), from December 2018 through October 2019.  
170 These image data were reduced to right ascension (RA) and declination (DEC) measure-  
171 ments as seen from the camera at the mid-exposure time. Details of the image reduc-  
172 tion process are presented by Liounis et al. (2019 in review, this collection), and here we  
173 provide only a summary.

174 The NavCam 1 images used for particle tracking were long-exposure images (typi-  
175 cally  $\sim 5$  s) that were intentionally designed to reveal background stars, leaving Bennu  
176 heavily over-exposed as a consequence. Initially these images were part of optical nav-  
177 igation image sequences, where the presence of stars allowed an accurate estimate of the

178 camera orientation for contemporaneous short-exposure images that revealed navigational  
179 landmarks on the surface of the asteroid. In later stages of the mission, image sequences  
180 dedicated to particle monitoring used only the long-exposure images.

181 A temperature-dependent focal plane distortion model was used for the NavCam  
182 1 images (Liounis et al., 2019 in review, this collection), while the image pointing solu-  
183 tion was obtained by matching cataloged reference stars to image sources. Image sources  
184 that reasonably matched a Gaussian point spread function and were not matched to a  
185 star were presumed to be candidate particle detections.

186 The active focal plane for NavCam 1 is  $2592 \times 1944$  pixels, leading to a field of view  
187 of  $44^\circ \times 32^\circ$ , given the  $288 \mu\text{rad}$  pixel scale ( $\sim 1$  arcmin) and accounting for optical dis-  
188 tortion (Bos et al., 2018). At typical spacecraft-particle distances of  $\sim 1$  km, this pixel  
189 scale translates to about 30 cm per pixel. Thus, given that the particle sizes are a few  
190 centimeters at most, the particles were not resolved in images. The point spread func-  
191 tion for particle detections typically has a full-width, half-max of  $\sim 1.7$  pixels (Hergenrother  
192 et al., 2019 in review, this collection).

193 The image processing approach (Liounis et al., 2019 in review, this collection) that  
194 we developed to mine the images for candidate particle detections was deliberately de-  
195 signed to ensure a high completeness, with the cost being a high rate of spurious detec-  
196 tions. From 1 December 2018 through 14 October 2019, the system identified  $\sim 18$  mil-  
197 lion candidate detections from 12640 images, for an average of 1400 detections per im-  
198 age. These potential detections include a large fraction of spurious detections that can  
199 arise from a variety of causes, including cosmic rays, the high background levels near Bennu's  
200 illuminated limb, unlinked stars, and camera artifacts such as stray light and hot pix-  
201 els. Based on visual inspection of images, we believe that only a few percent of such de-  
202 tections are not spurious.

203 The image processing pipeline assigns an integer quality code  $1 \leq Q \leq 5$  based  
204 on a variety of parameters including signal-to-noise ratio (SNR) and goodness of fit to  
205 a 2-dimensional Gaussian point spread function (Liounis et al., 2019 in review, this col-  
206 lection). Here  $Q = 1$  indicates a probably spurious detection (or a detection matched  
207 to a catalog star).  $Q = 2$  indicates a low-confidence detection that in many cases is as-  
208 sociated with a hot pixel or an unmatched star. Increasing values of  $Q$  denote increas-  
209 ing levels of confidence that the detection is associated with a particle.

210 The pipeline also assigns an astrometric error estimate to candidate detections, which  
211 is based heavily on the detection SNR (Liounis et al., 2019 in review, this collection).  
212 NavCam 1 significantly under-samples the point spread function (Bos et al., 2020, in press),  
213 and so the pipeline astrometric uncertainties are greater than would be expected for a  
214 well sampled detection. For our trajectory fits, we take a conservative approach, dou-  
215 bling the pipeline uncertainty and applying a floor uncertainty of 0.25 pixels. Figure 1  
216 shows the distribution of astrometric uncertainty used in the fits. The 0.25 pixel floor  
217 is clearly apparent in the plot, which cuts off at 5 pixels on the right. Less than 3% of  
218 detections have uncertainty over 5 pixels. The median uncertainty is 1.05 pixels.

219 The process of linking detections of a single object to produce a data set for or-  
220 bit estimation makes use of the intermediate linking step of the *track*. A track is a set  
221 of detections close together in time, covering up to a few hours duration, that are linked  
222 together by virtue of their compatible plane of sky motion. The track is generally com-  
223 posed of detections that approximately reflect uniform rectilinear motion on the sky. The  
224 tracks that we used for orbit estimation were largely derived from visual inspection and  
225 blinking of images, or through software tools. See Liounis et al. (2019 in review, this col-  
226 lection) and Hergenrother et al. (2019 in review, this collection) for details. If there are  
227 at least three detections in a track, it may be suitable for orbit fitting. The next level  
228 in the linking process is linking tracks of the same object, which we describe in Sec. 4.3.

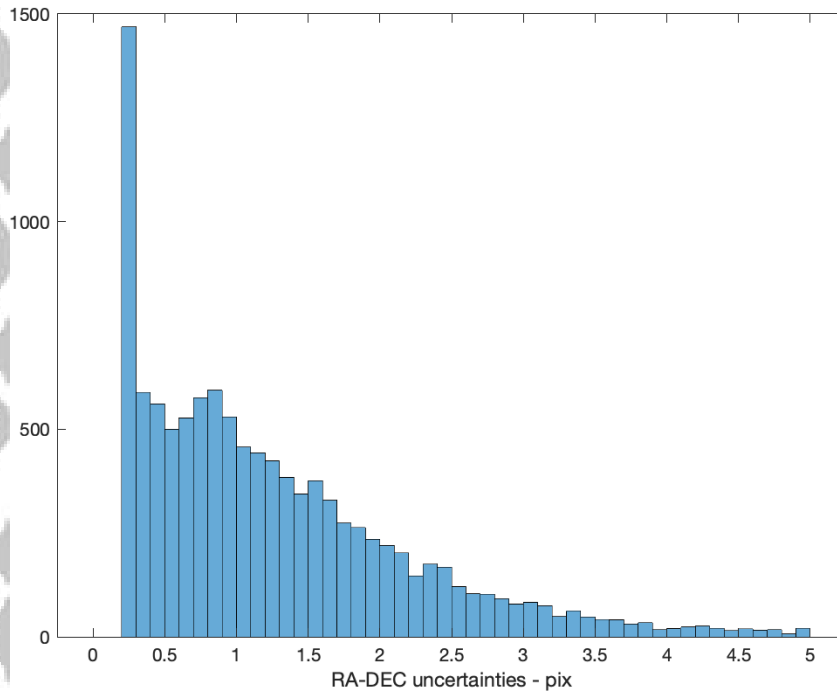


**Figure 1.** Distribution of RA and DEC uncertainties for the detections used in the trajectory fits.

229 The volume of detections is shown in Fig. 2, which shows clearly that only a tiny  
 230 fraction of candidate detections have been included in orbital fits. This is in part due  
 231 to the deliberately high rate of false detections, but the imaging cadence is also a deci-  
 232 sive factor. For example, the large number of detections in Orbital B (July 2019) was  
 233 acquired at a cadence and asteroid range that was unfavorable for linking more than two  
 234 detections into tracks (Hergenrother et al., 2019 in review, this collection), leaving many  
 235 unlinked pairs of detections. While these data may eventually be linked, it will require  
 236 more sophisticated algorithms (see, e.g., Denneau et al., 2013) than we have implemented  
 237 so far.

238 Lauretta et al. (2019) discuss the possibility that the OSIRIS-REx Laser Altime-  
 239 ter (OLA, Daly et al., 2017) may have detected particles in Bennu’s environment. We  
 240 have compared the off-Bennu returns reported by OLA with our particle trajectories,  
 241 but have not found a match. This only indicates that none of our particles are among  
 242 the ones possibly detected by OLA and does not imply that the reported off-Bennu OLA  
 243 detections were not associated with particles.

### 244 3 Force Models

245 Modeling the trajectory of a small particle moving in the Bennu environment re-  
 246 quires a detailed model of the forces acting on the particle. Table 1 lists the different forces  
 247 known to be acting on the particles. In addition to gravity, the effect of radiation pres-  
 248 sure on the particles is significant. Direct solar radiation pressure (SRP) is particularly  
 249 so, but more subtle effects such as radiation from Bennu and shadowing by Bennu can-  
 250 not be ignored.

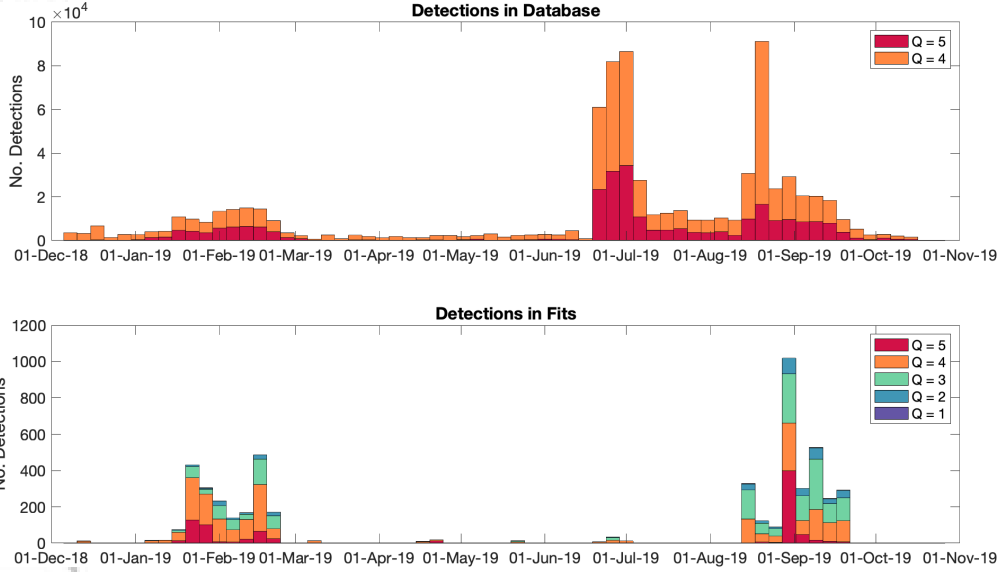


**Figure 2.** Times of detections present in pipeline database (upper panel) and used in orbital fits (lower panel).  $Q$  is a quality code, as described in the text, with larger values indicating higher confidence. In the upper panel we show only detections with  $Q \geq 4$  to improve clarity. Most orbit estimates were obtained from detections in the OSIRIS-REx Orbital A (January–February 2019) and Orbital C (August–September 2019) mission phases, when the spacecraft was orbiting at a radius of  $\sim 1.5$  km.

251 In the early stages of this effort, it proved difficult to fit the observational data, so  
 252 we worked to improve the force model fidelity as much as possible. And yet, there were  
 253 still clear signatures for unmodeled forces, which we were able to estimate. In the fol-  
 254 lowing subsections, we discuss the fundamental components of our force model, as well  
 255 as some small forces that may be acting but are not explicitly modeled. Detailed results  
 256 related to these models are discussed in Sec. 5.

### 257 3.1 Gravity

258 We modeled the gravitational acceleration for a particle in Bennu’s environment  
 259 through the classical spherical harmonic expansion with normalized coefficients  $C_{nm}$  and  
 260  $S_{nm}$ , where  $n$  and  $m$  are, respectively, the degree and order of the expansion (e.g., McMa-  
 261 hon et al., 2018). We also use the common notation for zonal terms in the expansion:  
 262  $J_n = -C_{n0}$ . Consistent with the circumscribing sphere of the Bennu shape model (Barnouin  
 263 et al., 2019), we used 290 m as the reference radius in the expansion. The sensitivity of  
 264 the particle trajectory allowed us to estimate not only the gravitational parameter  $GM$   
 265 of Bennu, but also many of the harmonic coefficients.

266 Our initial gravitational force model was based on the OSIRIS-REx shape model  
 267 (Barnouin et al., 2019), assuming uniform density (Werner, 1997). From this shape, we  
 268 derived the associated spherical harmonic coefficients and, as detailed in Sec. 4.2, we ap-  
 269 ply soft constraints to prevent the estimate from wandering farther from these values than  
 270 is required by the data.

271 Many of the particles spend a small fraction of their orbit beneath Bennu’s Brill-  
 272 ouin (circumscribing) sphere. We know that the standard spherical harmonic expansion



**Table 1.** Elements of the particle force model, including an approximate magnitude for a particle of area-to-mass ratio  $\eta = 0.075 \text{ m}^2/\text{kg}$  at an orbital radius of 500 m and above the subsolar point on Bennu when near perihelion.

Source of acceleration	Accel. ( $\text{km/s}^2$ )
Bennu point mass	$3 \times 10^{-8}$
Bennu gravitational harmonics	$6 \times 10^{-10}$
Direct solar radiation	$4 \times 10^{-10}$
Infrared emission from Bennu	$5 \times 10^{-11}$
Sunlight reflected from Bennu	$2 \times 10^{-11}$
Unmodeled forces	$< 1 \times 10^{-11}$
Reflected pressure: Direct solar	$3 \times 10^{-12}$
Reflected pressure: Infrared from Bennu	$3 \times 10^{-13}$
Reflected pressure: Sunlight from Bennu	$1 \times 10^{-13}$
Thermal emission from particle <sup>†</sup>	$\lesssim 8 \times 10^{-13}$
Solar tide	$5 \times 10^{-14}$
Poynting-Robertson Effect <sup>†</sup>	$4 \times 10^{-14}$

<sup>†</sup> — Not explicitly included in our force model.

273 does not converge globally beneath this sphere; however, the behavior of this divergence  
 274 is difficult to predict analytically and in general does not occur immediately at the Brillouin  
 275 boundary (Jekeli, 1983; Reimond & Baur, 2016). Thus we performed numerical tests  
 276 that compared the spherical harmonic model to the constant density polyhedron model  
 277 (Werner & Scheeres, 1996) to quantify this behavior. For the particular case of particles  
 278 orbiting about Bennu, we found that the effect due to divergence is small when compared  
 279 to truncation error at least up to degree 16, well beyond what can be inferred from  
 280 the particle detection data. This can likely be attributed to Bennu’s roughly spherical  
 281 shape. In the strictest sense it is the *infinite* series that is divergent, and we note that  
 282 the truncated series is smooth and continuous everywhere except at the expansion’s origin  
 283 (Bennu’s center of mass), which means that even if the truncated expansion does not  
 284 perfectly capture the dynamics, the partials needed for orbit determination and mapping  
 285 are still valid.

## 286 3.2 Radiation Pressure

### 287 3.2.1 Solar Radiation Pressure

288 The acceleration due to solar radiation impinging on a particle can be written as

$$\mathbf{a}_{\text{SRP}} = \Psi \eta \frac{\mathbf{r}_{\odot}}{r_{\odot}^3},$$

289 where  $\mathbf{r}_{\odot}$  is the vector from the Sun to the particle and  $\eta$  is the ratio of cross-sectional  
 290 area to mass for the particle. Radiation pressure from photons reflected or scattered by  
 291 the particle is discussed below. For this work, we take a solar irradiance of  $1367 \text{ W/m}^2$   
 292 (Fröhlich & London, 1986), leading to a solar radiation pressure constant  $\Psi = 1.016 \times$   
 293  $10^{17} \text{ N}$  and associated SRP of  $4.56 \mu\text{Pa}$  at 1 au.

294 If we consider a notional spherical particle of 1 cm in diameter and a bulk density  
 295 of  $2 \text{ g/cm}^3$ , then we have  $\eta = 0.075 \text{ m}^2/\text{kg}$ . Given the orbit of Bennu, SRP on our notional  
 296 particle causes an acceleration ranging from a peak of  $4.2 \times 10^{-10} \text{ km/s}^2$  at perihelion  
 297 (0.90 au) down to  $1.8 \times 10^{-10} \text{ km/s}^2$  at aphelion (1.36 au). As we shall see below,  
 298 the trajectories of many particles are strongly sensitive to this acceleration.

299 Many particles enter Bennu’s shadow, during which time SRP is not acting. We  
 300 implement a high-fidelity shadowing model based on the detailed shape of Bennu. When  
 301 the Sun is fully eclipsed by Bennu, as seen by the particle, SRP is neglected. When the  
 302 Sun is partially eclipsed by Bennu, the fraction of the solar disk visible from the parti-  
 303 cle serves as a scale factor on SRP. We do not shift the direction of SRP during partial  
 304 eclipse to account for the slightly offset centroid of the visible Sun.

305 Our model assumes a constant value of  $\eta$ , which we consider to be a reasonable ap-  
 306 proach given that the particles must be rapidly tumbling for any realistic partition be-  
 307 tween translational and rotational kinetic energy. Thus, while the instantaneous value  
 308 of  $\eta$  may be evolving rapidly on short time scales ( $\sim 1$  s), a useful mean can be obtained  
 309 with relatively short averaging intervals, far less than the time span of our observational  
 310 data (hours to days).

### 311 3.2.2 Bennu Radiation Pressure

312 In addition to radiation arriving directly from the Sun, other solar radiation reaches  
 313 the particles indirectly, most notably from the surface of Bennu. This comes in two forms,  
 314 namely reflected solar radiation and thermal emissions due to solar heating of the Bennu  
 315 surface.

316 For solar radiation reflected from Bennu to the particle, often referred to as the *albedo*  
 317 *effect*, we do a facet-wise summation of the reflected radiation for all Bennu facets that  
 318 are visible to both the particle and the Sun. For a uniform geometric albedo  $\mathcal{A}$  and lam-  
 319 bertian scattering, this can be written as (Borderies & Longaretti, 1990)

$$\mathbf{a}_{\text{albedo}} = \frac{\mathcal{A}\Psi\eta}{\pi r_{\odot}^2} \sum_{i \in \mathcal{I}} A_i \cos \gamma_i \cos \alpha_i \frac{\mathbf{r}_i}{r_i^3},$$

320 where the area of the  $i$ th facet is denoted by  $A_i$ . Here  $\gamma_i$  is the emission angle from the  
 321 center of the  $i$ th facet to the particle, i.e., the angle between the facet unit normal vec-  
 322 tor  $\hat{\mathbf{n}}_i$  and the vector  $\mathbf{r}_i$  from the facet center to the particle. Thus  $\cos \gamma_i = \hat{\mathbf{n}}_i \cdot \mathbf{r}_i / r_i$ .  
 323 Similarly,  $\alpha_i$  is the solar incidence angle at the  $i$ th facet, so  $\cos \alpha_i = -\hat{\mathbf{n}}_i \cdot \mathbf{r}_{\odot} / r_{\odot}$ . The  
 324 facets to be included in the summation are denoted by  $\mathcal{I}$ , which is the set of facet in-  
 325 dices for which both  $\cos \gamma_i$  and  $\cos \alpha_i$  are positive.

326 For the infrared radiation pressure (IRP) from Bennu, surface temperatures were  
 327 generated by the Advanced Thermophysical Model (ATPM) of Rozitis and Green (2011,  
 328 2012, 2013) using the thermophysical properties of Bennu derived by Dellagiustina et  
 329 al. (2019). The ATPM returns an interpolated temperature  $T_i$  at the  $i$ th facet from a  
 330 look-up table of temperatures for each facet as a function of the local solar time in  $1^\circ$   
 331 steps. The effect of varying heliocentric distance  $r_{\odot}$  from the reference value of the in-  
 332 terpolation table  $r_{\odot\text{REF}}$  was captured by scaling the reference temperature  $T_{\text{REF}}$  accord-  
 333 ing to  $(T/T_{\text{REF}})^4 = (r_{\odot\text{REF}}/r_{\odot})^2$ . Now, with the temperature at each facet from the  
 334 look-up table, we can compute the IRP acceleration as a sum over all facets visible to  
 335 the particle:

$$\mathbf{a}_{\text{IRP}} = \frac{\sigma\epsilon\eta}{c\pi} \sum_{i \in \mathcal{I}} T_i^4 A_i \cos \gamma_i \frac{\mathbf{r}_i}{r_i^3},$$

336 where  $\sigma$  is the Stefan-Boltzmann constant,  $\epsilon$  is the Bennu emissivity (assumed to be 0.9  
 337 everywhere), and  $c$  is the speed of light. Here  $\mathcal{I}$  is the set of facet indices for which  $\cos \gamma_i >$   
 338 0.

339 This IRP model breaks down when the particle altitude is comparable to or be-  
 340 low the shape model facet scale. We work past this problem by applying the force ob-  
 341 tained at an altitude of 10 m whenever the particle falls below 10 m altitude. Altitudes  
 342 below 10 m are rare and brief events, typically seen only in the few tens of seconds af-

343 ter ejection or before impact, and we do not consider this to be a significant source of  
 344 force modeling error.

345 For both of these sources of radiation, albedo and IRP, we use the same polyhe-  
 346 dral shape model mentioned above (Barnouin et al., 2019) to compute the associated-  
 347 color acceleration. For our fits, we used a shape version with 3072 facets (mean facet edge  
 348  $\sim 25$  m), though we did test a variant with  $4\times$  more facets (12288 facets, mean edge length  
 349  $\sim 12.6$  m) and found that the results did not depend upon which of the two models was  
 350 used.

### 351 **3.2.3 Reflected Radiation Pressure**

352 The photons that impinge on a particle are responsible for direct radiation pres-  
 353 sure, as discussed above for SRP, IRP, and the albedo effect. But some fraction of the  
 354 photons that strike the particle are reflected or scattered away, leading to additional mo-  
 355 mentum transfer, which we refer to as *reflected radiation pressure*. Photons not reflected  
 356 are absorbed, thus heating the particle, leading to subsequent emission of thermal pho-  
 357 tons. Here we discuss the momentum transfer due to reflected photons, and in Sec 3.2.4  
 358 we will discuss the possibility of accelerations due to thermal emission from the parti-  
 359 cle.

360 We do not have detailed models for the particle shapes, albedos, or light-scattering  
 361 properties, so we adopt a simple model assuming spherical particles with lambertian scat-  
 362 tering. Under these assumptions, the ratio of reflected to direct radiation pressure is  $\frac{4}{9}\mathcal{A}_{\text{Bond}}$ ,  
 363 where  $\mathcal{A}_{\text{Bond}}$  is the Bond albedo (Borderies & Longaretti, 1990). Thus the total radi-  
 364 ation pressure from a given source is

$$\mathbf{a}_{\text{TOTAL}} = \left(1 + \frac{4}{9}\mathcal{A}_{\text{Bond}}\right) \mathbf{a}_{\text{DIRECT}}.$$

365 Here  $\mathbf{a}_{\text{DIRECT}}$  can alternately refer to  $\mathbf{a}_{\text{SRP}}$ ,  $\mathbf{a}_{\text{IRP}}$  or  $\mathbf{a}_{\text{albedo}}$ , depending on the radiation  
 366 source under consideration. We further assume  $\mathcal{A}_{\text{Bond}} = 0.016$  (Dellagiustina et al., 2019)  
 367 so that reflected radiation pressure is 0.7% of the direct radiation pressure. As part of  
 368 our orbit determination approach (discussed in Sec. 4.2), we estimate the total radi-  
 369 ation pressure by estimating the value of the term  $\eta' = (1 + \frac{4}{9}\mathcal{A}_{\text{Bond}})\eta$ . Thus, when de-  
 370 riving area-to-mass ratios of the particles, we scale the estimated parameter to obtain  
 371  $\eta = \eta'/1.007$ .

372 We emphasize that there are several crucial and untested assumptions that go into  
 373 our assessment of reflected radiation pressure. As mentioned above, we can reasonably  
 374 suppose that the particles are rapidly tumbling, and thus shape effects could be effec-  
 375 tively modeled by a mean  $\eta$ , but the scattering properties and albedo are unknown. This  
 376 could introduce a bias in our estimates of  $\eta$ , but should still allow the orbit estimation  
 377 approach to obtain the correct  $\eta'$  and total acceleration  $\mathbf{a}_{\text{TOTAL}}$ , which is important for  
 378 the overall trajectory estimate.

### 379 **3.2.4 Particle Thermal Emissions**

380 It is well known that the Yarkovsky effect, a subtle acceleration due to the reac-  
 381 tion force from thermal emission, can significantly alter an asteroid's heliocentric orbit  
 382 over long time scales (see, e.g., Bottke et al., 2006; Vokrouhlický et al., 2015). Here we  
 383 consider the possibility that thermal emission from particles may also affect their tra-  
 384 jectories in an appreciable way.

385 The Yarkovsky effect depends nonlinearly on the rotation rate of the body in ques-  
 386 tion, and yet our data provide no direct constraint on the particle rotation periods (Hergenrother  
 387 et al., 2019 in review, this collection). We do presume, however, that the partition be-  
 388 tween translational and rotational kinetic energy is not extreme. For a typical 1 cm par-

389 ticle with ejection velocity of the order of 20 cm/s, the rotation period must be less than  
 390 1 s, assuming that at least 1% of the particle kinetic energy is due to rotation. Taking  
 391 an equipartition between translational and rotational kinetic energies yields a rotation  
 392 period of 0.1 s, corresponding to the shortest periods considered here.

393 Such high spin rates raise the question of whether particles should be expected to  
 394 have the strength to avoid rotational bursting. Sánchez and Scheeres (2014) provide an  
 395 expression for the failure spin rate of an idealized body held together by self gravity and  
 396 cohesion. This allows them to bound the cohesive strength  $\sigma$  of a rapidly spinning particle  
 397 according to

$$\sigma > \frac{\rho d^2}{4} \left[ \omega^2 - \frac{4\pi G \rho}{3} \right]$$

398 where  $\omega$  is the rotation rate,  $\rho$  is the density of the particle,  $d$  is its diameter and  $G$  is  
 399 the gravitational constant. For our presumed spin rates and reasonable meteorite bulk  
 400 densities the gravitational term,  $4\pi G \rho / 3$ , is orders of magnitude less than the rotational  
 401 term,  $\omega^2$ , and can be neglected. Thus the strength limit can be simplified to  $\sigma > \rho d^2 \omega^2 / 4$ .  
 402 Then, assuming a particle of diameter 1 cm and density of 2000 kg/m<sup>3</sup> spinning at pe-  
 403 riods from 0.1–1 s, the minimum particle strength must be in the range 2–200 Pa, far  
 404 below the cohesive strengths of meteorites which, at smallest, are at the several kPa level  
 405 (Scheeres et al., 2015). Thus, the particle need not have much strength to hold together.

406 Returning to the Yarkovsky modeling, we used a simple approach based on linearized  
 407 heat conduction theory. Assuming spherical and homogeneous particles, Vokrouhlický  
 408 (1998) estimated thermal accelerations based on rotational cycling (diurnal effect; in this  
 409 crude estimate, we neglect the seasonal effect). For quantitative conclusions, we adopted  
 410 a thermal inertia of 350 J m<sup>-2</sup> K<sup>-1</sup> s<sup>-1/2</sup>, roughly corresponding to the pebble compo-  
 411 nent of Bennu’s surface, and a thermal conductivity of 0.1 W m<sup>-1</sup> K<sup>-1</sup>. To maximize  
 412 the role of the diurnal thermal component, we assumed the instantaneous location of the  
 413 Sun at the particle’s equator (in the plane perpendicular to the instantaneous rotation  
 414 axis). We tested particle sizes between 1 and 10 cm and assumed their rotation period  
 415 ranged between 0.1 and 10 seconds.

416 With these parameters set, the penetration depth of the diurnal thermal wave ranges  
 417 between about a millimeter (for the shortest periods) to a little less than a centimeter  
 418 (for the longest periods; top panel on Fig. 3). The particles are thus barely in the large-  
 419 body regime, with the exception of the slowly rotating centimeter-sized particles, which  
 420 are already in the small-body regime (thus efficiently conducting heat throughout their  
 421 volume). In the high-inertia situation considered here, the diurnal thermal parameter  
 422 ranges between several tens (for the longest periods) to several hundreds (for the short-  
 423 est periods), implying rather efficient longitudinal equalizing of temperature (see, e.g.,  
 424 Bottke et al., 2006; Vokrouhlický et al., 2015). This is the principal reason for making  
 425 the total thermal acceleration very small for the short rotation periods.

426 Figure 3, bottom panel, shows the total thermal acceleration expressed as a frac-  
 427 tion of the direct SRP for various particle sizes and as a function of the rotation period.  
 428 Given that particle spin periods should be <1 s, the fraction is only  $\lesssim 2 \times 10^{-3}$ , quite  
 429 small compared to other forces at play. For all combinations in our parameter space, this  
 430 fraction ranges between  $\simeq 0.001$  and  $\simeq 0.01$ . Even extending the rotation periods by  
 431 an order of magnitude larger, the computed fraction of the thermal acceleration stalls  
 432 at a few percent of SRP. This is because in that case the thermal penetration depth be-  
 433 comes comparable to, or larger than, the particle sizes, and the heat conduction across  
 434 the particles equalize the surface temperature.

435 The take-away message is that thermal recoil acceleration on particles is  $\sim 3$  orders  
 436 of magnitude less than SRP, and roughly an order of magnitude less than reflected so-  
 437 lar radiation. We neglect this as a source of acceleration in our dynamical model.

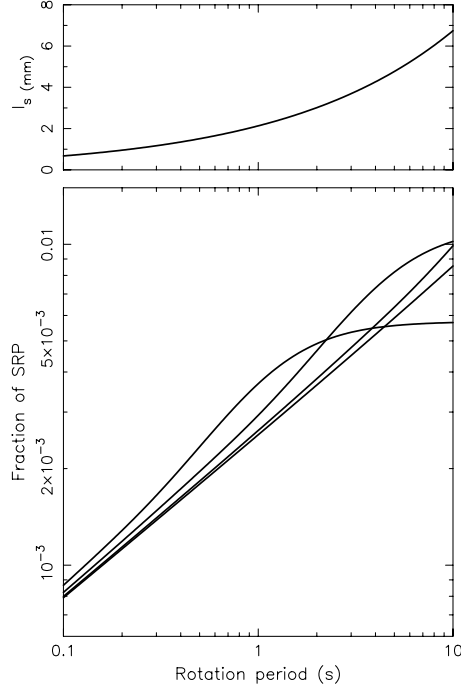


**Figure 3.** Top panel: Skin depth  $\ell_s$  for the diurnal thermal wave as a function of rotation period. Bottom panel: Thermal recoil acceleration as a fraction of direct SRP versus rotation period. The lower plot assumes spherical particles of diameters 1, 2, 5, and 10 cm (from upper to lower curve at left of plot).

438

### 3.3 Other Known Accelerations

439

440

441

442

443

The third-body gravitational perturbation from the Sun can be cast as the differential acceleration between a particle near Bennu and Bennu itself, also known as solar tide. For a particle  $\sim 0.25$  km above the subsolar point on Bennu when at perihelion, this acceleration is roughly  $5 \times 10^{-14}$  km/s<sup>2</sup>. We include this term in our force model, despite the fact that it is not a significant perturbation for the particles.

444

445

446

447

448

Poynting-Robertson acceleration is a very slight acceleration related to SRP. Stellar aberration related to the velocity  $v$  of the observer moves the apparent place of the Sun by an angle of order  $v/c$ , for an observer on a circular orbit. This leads to a transverse acceleration  $\sim 10^{-4}$  of SRP, or  $\sim 4 \times 10^{-14}$  km/s<sup>2</sup> for a particle near Bennu at perihelion. Our force model neglects this perturbation.

449

### 3.4 Empirical Accelerations

450

451

452

453

454

455

456

As we discuss in more detail below, the elements of the force model discussed so far did not lead to reasonable postfit residuals of the astrometric data. Given this inability to match the observations to an integrated trajectory, it became clear that either mismodeling of the observations was responsible or there were unmodeled forces at play. After carefully verifying the observation model, and accounting for observation model uncertainties, we concluded that additional accelerations of order  $10^{-12}$  km/s<sup>2</sup> to as much as  $10^{-11}$  km/s<sup>2</sup> were acting on the particles. In a later section we discuss in greater de-

457 tail the orbit determination approach, but here we describe our model for empirical ac-  
458 celerations.

459 The empirical acceleration model assigns an acceleration vector  $\mathbf{a}_i = \mathbf{a}(t_i)$  at a  
460 series of times  $t_i$  spanning the observation interval. The times  $t_i$  are arbitrary, but in prac-  
461 tice we select a constant time interval  $\Delta t$  so that  $t_{i+1} = t_i + \Delta t$ . The acceleration at  
462 times between the  $t_i$  nodes are obtained through linear interpolation, according to

$$\mathbf{a}(t) = \mathbf{a}_i + \frac{\mathbf{a}_{i+1} - \mathbf{a}_i}{\Delta t}(t - t_i) \text{ for } t \in [t_i, t_{i+1}] .$$

463 Because the empirical acceleration model is continuous in time, it does not pose diffi-  
464 culty for our particle integrator, which requires an integrator restart at all discontinu-  
465 ities.

466 The components of each  $\mathbf{a}_i$  are estimable parameters, with *a priori* constraints. Es-  
467 timating these empirical acceleration parameters serves to ensure that the modeled tra-  
468 jectory of the particle allows it to reach the location where it was observed to be, and  
469 thus allows fits consistent with the observational uncertainty. In cases where there are  
470 extended time gaps in observation coverage, the  $\mathbf{a}_i$  implement what can be considered  
471 the minimum thrust transfer from the time of the earlier observation to the time of the  
472 later observations.

## 473 4 Orbit Estimation Approach

### 474 4.1 Initial Orbit Determination

475 Linked sets of observations (single tracks) with at least three detections are fed into  
476 a three-stage orbit determination process. The first stage is the initial orbit determina-  
477 tion (IOD). Initially, nothing is known about a particle's orbit, other than that it pro-  
478 duced the observations (assuming the associations are correct). The role of IOD is to gen-  
479 erate one or more candidate trajectories that could have produced the observations. There  
480 are many classes of IOD algorithms that have been designed for various orbital problems.  
481 Here, we use a general-purpose IOD algorithm that performs a grid search/simplex op-  
482 timization over a range of orbital elements to minimize the RMS of the observation resid-  
483 uals. This method is robust in the sense that it explores a wide range of possible orbits  
484 and in the sense that it is not limited by any observability constraints (i.e., it is insen-  
485 sitive to observing geometry). It is also relatively quick to converge because it only deals  
486 with Keplerian dynamics. However, in some cases, particularly when there are few (e.g.,  
487 three to five) detections, the algorithm will converge to an erroneous local minimum that  
488 may be far from the true solution. Typically, this can only be determined to be the case  
489 with the addition of more observations, or through the use of some external criteria (i.e.,  
490 dynamical arguments, visual inspection, etc). Tracks that could not be fit with resid-  
491 ual RMS < 8 pixels were rejected from consideration.

### 492 4.2 Orbit Determination

493 Next, the resultant IOD solution is fed into a more conventional orbit determina-  
494 tion (OD) software suite derived from JPL's Orbit Determination Program (MIRAGE/ODP)  
495 that is better tuned for satellite ephemeris estimation. This step performs iterative dif-  
496 ferential corrections to the trajectory to minimize the sum of the squares of the obser-  
497 vation residuals. In particular, it implements a batched sequential weighted square root  
498 information filter (SRIF) that supports stochastic parameter estimation (white noise or  
499 exponentially correlated). This and similar algorithms are well documented in the lit-  
500 erature (e.g., Tapley et al., 2004; Bierman, 1977; Moyer, 2003) and have been at the heart  
501 of orbit determination for the past several decades. It is at this stage where higher-fidelity  
502 force modeling is added and *a priori* uncertainties are applied.

503 In a system that is well constrained by the observational data, the *a priori* uncer-  
 504 tainty can be set to infinity (i.e., zero *a priori* information) and the filter will converge,  
 505 provided the initial IOD estimate is within the linear regime of the correct solution. How-  
 506 ever, when fitting a single track (with few detections) to an orbit, the system can be poorly  
 507 constrained by the observations, often because there are one or more linear combinations  
 508 of the components of the state vector that are unobservable. In practice, this typically  
 509 results in filter divergence, which can be mitigated by constraining the estimated param-  
 510 eters to the IOD solution through the use of suitable *a priori* covariance matrix, which  
 511 enforces the hypothesis that the IOD solution is approximately correct. Here, we set the  
 512 *a priori* constraints based on the scale of the Bennu system. Each component of the par-  
 513 ticle’s position is assigned a 250 m *a priori* uncertainty, which in three dimensions roughly  
 514 equates to Bennu’s volume. Each component of the particle’s velocity is assigned a 30  
 515 cm/s *a priori* uncertainty, which is the same order of magnitude as the escape speeds  
 516 on Bennu’s surface. It was deemed that if the IOD solution could not be trusted at this  
 517 level, then that IOD solution was not useful as a starting solution. In the vast major-  
 518 ity of cases, the total correction from the IOD solution at the filter epoch was less than  
 519 50 m, with the data driving the *a posteriori* uncertainty.

520 The area-to-mass ratio for each particle was estimated with an *a priori* constraint  
 521 set to  $\eta = 0.08 \pm 0.1 \text{ m}^2/\text{kg}$ , which corresponds to a 0.9 cm particle with  $2000 \text{ kg/m}^3$   
 522 density. The constraint allows the solution to readily move close to zero (representing  
 523 large particles), but constrains  $\eta < 0.38 \text{ m}^2/\text{kg}$  (size larger than  $\sim 2 \text{ mm}$ ) at 3-sigma.

524 The particle trajectories are propagated using a  $16 \times 16$  spherical harmonic grav-  
 525 ity field. Nominally, the gravity field is not estimated. Of the few hundred particles that  
 526 have been fit, about 20 contain valuable gravity information. These particles were fit si-  
 527 multaneously to produce a single, combined estimate of the gravity field as described in  
 528 Sec. 5.6 below. This gravity field was then fed back in to the rest of the particle solu-  
 529 tions.

530 Empirical accelerations were modeled as described in Sec. 3.4, and the nodes  $\mathbf{a}_i$  of  
 531 the linearly interpolated accelerations were estimated. We chose a 1-hour spacing be-  
 532 tween nodes to capture any unmodeled dynamics at finer temporal resolution than the  
 533 typical particle orbital period. The *a priori* uncertainty of each node was set to  $10^{-11} \text{ km/s}^2$ ,  
 534 somewhat more than the net acceleration due to reflected radiation pressure. We believe  
 535 this choice to be conservative given that the majority of particles, particularly shorter-  
 536 lived particles, do not require any miscellaneous accelerations, and the set of longer lived  
 537 particles that do generally only require accelerations on the order of a few times  $10^{-12}$   
 538  $\text{km/s}^2$ , which is well below the *a priori* uncertainty. This results in larger *a posteriori*  
 539 uncertainties for the estimated parameters.

540 The final set of estimated parameters are stochastic corrections to the spacecraft  
 541 trajectory. The spacecraft trajectory is assumed to be accurate to  $\pm 50 \text{ cm}$ , 1-sigma, and  
 542 corrections are estimated in the Bennu-centered radial-transverse-normal (RTN) frame  
 543 in 1-hour batches, correlated exponentially with a time constant of 4 hours to prevent  
 544 blatantly discrete, nonphysical jumps. With these settings, we estimate sub-sigma cor-  
 545 rections to the spacecraft trajectory at all times.

546 The empirical accelerations and the estimated corrections to the spacecraft trajec-  
 547 tory are in tension with each other in the OD process, and there was the risk that ei-  
 548 ther or both might alias with the gravity field. To characterize these concerns we per-  
 549 formed tests in which we varied the balance of relative *a priori* uncertainties between the  
 550 empirical accelerations and spacecraft position errors. Loosening the *a priori* constraints  
 551 on the spacecraft trajectory did not effect either the miscellaneous forces or the grav-  
 552 ity field and the trajectory corrections remained bounded at  $< 50 \text{ cm}$ . Tightening the  
 553 *a priori* constraints on the spacecraft trajectory added structure to the residuals and gen-

554 erally increased the magnitude of miscellaneous forces, however the gravity field remained  
555 unaffected.

556 On the other hand, tightening the *a priori* constraints on the miscellaneous forces  
557 also resulted in structured residuals and caused multi-meter corrections to the spacecraft  
558 trajectory. In this case GM increased a few sigma, however this also did not have a large  
559 effect on the harmonic coefficients. Moreover, we found no appreciable correlations be-  
560 tween the miscellaneous forces and any of the harmonic coefficients when inspecting the  
561 estimated covariance matrices. This is not particularly surprising in light of the fact that  
562 our gravity estimate (Sec. 5.6) is based on a simultaneous fit of numerous particles. For  
563 an individual particle fit, empirical forces could more readily alias with gravity signals,  
564 but with multiple particles this risk is significantly diminished because the common grav-  
565 ity field cannot be significantly skewed by the empirical forces of a single particle. And  
566 since the empirical accelerations are estimated parameters, any correlation with the grav-  
567 ity field would manifest as increased uncertainty on the gravity coefficients. Thus the  
568 incorporation of empirical accelerations serves to weaken the gravity field estimate in an  
569 appropriate way.

570 To minimize linearization errors associated with the differential correction, both  
571 the numerical integration and filtering epochs are chosen to be near the mean of the ob-  
572 servation times. This requires that the integration is performed in two legs—a backward  
573 leg and a forward leg—the result of which is that the total duration over which nonlin-  
574 ear effects could manifest is halved. This has the primary effect of reducing the num-  
575 ber of iterations needed for convergence, and it also allows for the fitting of longer-duration  
576 arcs.

### 577 4.3 Orbit Linkage

578 The final stage of the particle orbit determination is the track association, which  
579 is the process of determining which tracks belong to the same object and refitting the  
580 trajectories accordingly. Linkages were obtained either through *orbit identification* (Milani  
581 et al., 2000) by virtue of orbital similarity in cases where both tracks had fitted orbits,  
582 or by *attribution* (Milani et al., 2001) if only one track had a successful orbit estimate.

583 For orbit identification, the best fit trajectories for each track were compared to  
584 one another in a statistical sense. For each pair of tracks, the trajectory and uncertainty  
585 of both tracks were propagated to their mid-time (provided both trajectories exist at this  
586 time). The combined Mahalanobis distance,  $\mathcal{D}$ , was then computed as

$$\mathcal{D} = \sqrt{\delta\mathbf{x}^T P^{-1} \delta\mathbf{x}}$$

587 where  $\delta\mathbf{x} = \mathbf{X}_2 - \mathbf{X}_1$  is the difference between the 6-dimensional position and velocity  
588 states and  $P = P_1 + P_2$ , the sum of the mapped covariance matrices, is the combined  
589 state uncertainty in both orbits.  $\mathcal{D}$  is a direct, scalar measurement of the likeness of two  
590 orbits in units of standard deviation. We found that, in general, orbit pairs with  $\mathcal{D} \lesssim$   
591 2 were in fact the same object.

592 Then, we performed attribution, which involved propagating a fitted track’s tra-  
593 jectory and uncertainty to the mid-time of another track, rotating the state uncertainty  
594 into the OSIRIS-REx spacecraft’s plane of sky, and computing the Mahalanobis distance  
595 in the 4-dimensional space of right ascension, declination, and their rates. We computed  
596 the observed plane of sky position and velocity at the midpoint via interpolation. This  
597 method has the advantage of only requiring one of the two tracks to have a determined  
598 orbit, which provided the opportunity for tracks that failed during IOD/OD or tracks  
599 that have less than 3 detections to be linked.

600 While we relied heavily on the tracks that were formed by linking detections, as  
601 described by Hergenrother et al. (2019 in review, this collection) and Liounis et al. (2019



in review, this collection), we also attributed 861 previously unlinked detections by scanning the entire detection database for sets of unlinked detections that were close to the predicted position for a given particle. Typically we would add the new detections to an existing track, though in many cases we formed a new track from the attributed detections. We have so far not gone back to the images to search for detections not in the database. This approach might be occasionally successful, especially for ruling out potentially spurious orbital solutions, but as mentioned in Sec. 2, our detection database is deliberately very complete at the cost of having a low purity.

Once the links were made, the OD and association process was iterated until no further links were found. However, there are likely a few missing links within our catalog, as we know the orbit identification and attribution algorithms are not foolproof. We did perform visual inspections of both the trajectories and the residuals to catch any obvious links that were missed. Most of these were easily fed back into the OD; however, we found a few that we believe to be related that at time of this writing have proved difficult to fit together (e.g., P249  $\leftrightarrow$  P252, P294  $\leftrightarrow$  P303, P289  $\leftrightarrow$  P302 and P31  $\leftrightarrow$  P153). Each of these particle pairs appear to be in remarkably similar orbits and are photometrically consistent, but according to our *orbit identification* tests they are statistically very different ( $\mathcal{D} \gg 10$ ) and when we try to fit them together we estimate significantly larger ( $\sim 2\text{--}10\times$ ) miscellaneous forces than we do in the individual solutions. This may be an indication of an impulsive change in the orbit as would be seen, e.g., for fissioning of grains from the particle, but for the present we leave these particles unlinked as we continue to investigate their relationship.

## 5 Results and Discussion

Our approach has been to estimate a trajectory for each of the 517 tracks that have been visually validated and that have  $N_{\text{det}} \geq 3$ . From among these, there were a modest number ( $\sim 25$ ) of failures in IOD or OD, in many cases because the IOD returned a solution in an erroneous local minimum. Overall, this approach led to successful fits for 390 objects comprising 488 tracks. From among these, we excluded from the following analysis those particles for which we are doubtful that the fit is reliable owing to, e.g., a poor fit to the data, a weak orbital solution or an orbital solution that appears erroneous. More specifically, we considered the fit too poor if the weighted RMS (WRMS) of postfit residuals exceeded unity, and we judged the solution controlled too much by the *a priori* constraint (and not enough by the data) if the maximum eigenvalue of the  $3 \times 3$  position covariance matrix was more than 90% of the 250 m *a priori* constraint. We also excluded cases where particle trajectories appeared nonphysical, e.g., cases where the estimated trajectory showed the particle was occulted by Bennu at the time of any detections, or cases that appeared to arrive from infinity. The cases that arrived from infinity did so at low velocities, 1 m/s or slower, and thus are related to Bennu and not interplanetary passersby. Moreover, their orbital geometries were inconsistent with particles that were "blown" back into the Bennu vicinity by SRP. Finally, we excluded several cases where the particle was traveling on a low-eccentricity orbit and unusually close to the spacecraft at the time of observations, which is an *a priori* unlikely solution that often indicates that the solution is in the wrong local minimum. Together these exclusions removed 77 cases from consideration, leaving 313 particle trajectories for the analysis that follows.

In an external data repository we provide a catalog of these 313 trajectory estimates (Chesley et al., 2019). In what follows, we prepend a "P" to the Object Number designation from this catalog to form an identifier for individual particles. For example "P100" refers to Object Number 100 from the catalog.

Altogether, our 313 particle trajectories are based on 409 distinct tracks and 5087 detections. For 36 particles, we were able to link multiple tracks to form a larger data

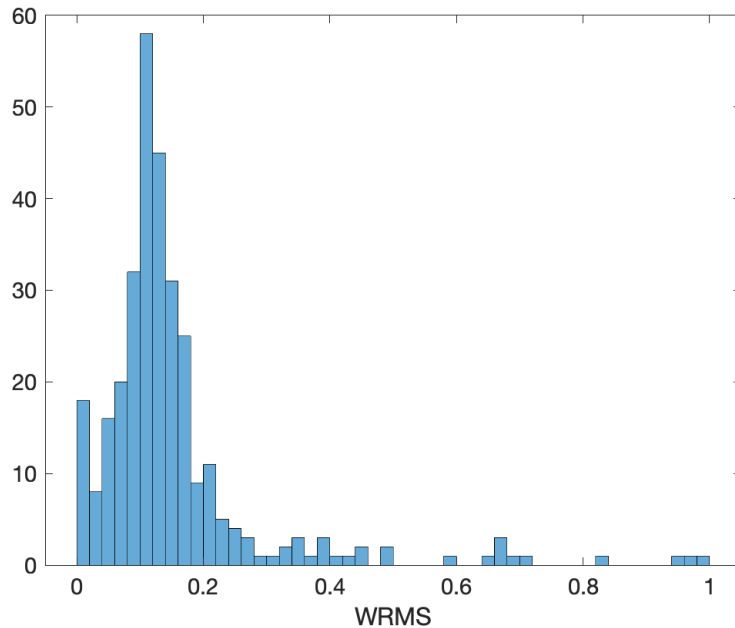


**Figure 4.** Weighted RMS of postfit residuals for 313 particle trajectory fits.

653 set. Most often this consisted of linking only two tracks together, but in seven cases we  
 654 were able to link six or more tracks, including one case (P2) with 15 tracks altogether.  
 655 All told we were able to link a total of 96 additional tracks to existing objects, includ-  
 656 ing a few tracks with only two detections.

657 Figure 4 depicts the distribution of WRMS for our 313 fits. The distribution is strongly  
 658 skewed towards zero and away from the idealized value of unity, indicating that the data  
 659 are underweighted, which we consider desirable given the presence of systematic errors  
 660 in the dynamical and observational models, as well as the extraordinary flexibility built  
 661 into the solution process through the estimation of empirical accelerations and space-  
 662 craft position errors (as described in Sec. 4.2). The distribution suggests that some of  
 663 the fits with  $WRMS > 0.5$  may also be spurious. Indeed, while we are confident that  
 664 the vast majority of our fits are reliable, there are likely a few apparently valid and yet  
 665 spurious solutions, but given the large data set at hand, this does not compromise the  
 666 overall analysis. Validating these solutions and incorporating additional data are ongo-  
 667 ing efforts.

668 The observed arc for most particles is fairly short, with 114 particles (36%) hav-  
 669 ing data sets covering  $< 1$  h and only 10 extending over 24 h in duration. At 5.5 days,  
 670 P1 has the longest observed arc. The number of detections ranges as high as  $N_{\text{det}} = 378$   
 671 for P247, and we have 13 particles for which  $N_{\text{det}} > 50$ . (See Fig. 5.)

672 We find that 259 (83%) of our particle trajectories have both ejection and impact  
 673 within 7 days of the detection set, and hence a finite lifetime. Figure 6 shows the dis-  
 674 tribution of these cases, among which 80% have lifetime shorter than a day and the me-  
 675 dian lifetime is 0.23 days. The maximum lifetime is 6.7 days, but we emphasize that for  
 676 17% of objects we do not identify an ejection or impact or both, meaning that a lifetime  
 677 could not be determined. For such cases with an identified ejection or impact, the nom-  
 678 inal lifetime would be upwards of 7 days, and at least 14 days otherwise. However, most  
 679 cases with indefinite lifetime are dominated by orbital uncertainties, and we expect that  
 680 many are in fact relatively short lived. Overall, these results are consistent with the Monte

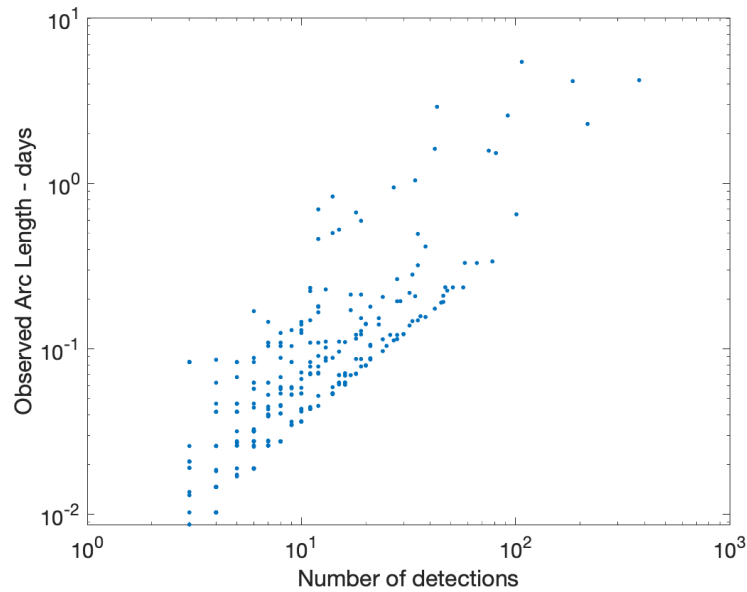


**Figure 5.** Arc length vs. number of detections for particle trajectory fits.

681 Carlo-like approach taken by McMahon et al. (2019 in review, this collection), who found  
 682 only 10% of their non-random samples remained aloft and near Bennu for longer than  
 683 7 days.

### 684 5.1 Orbital Types

685 We can categorize our particle trajectories according to their orbital type: either  
 686 suborbital, orbital or escaping. The key parameter that determines into which category  
 687 a particles falls is the velocity (magnitude and direction) at ejection. Slower velocities  
 688 will tend towards sub-orbital and faster velocities will tend towards escape, with the ob-  
 689 jects experiencing multiple orbital revolutions falling in between.

690 A particle's periapsis radius is necessarily below the surface at ejection, and so un-  
 691 der the naive assumption of Keplerian motion about a spherical body, there can be no  
 692 multi-revolution objects. But under a more realistic dynamical model, those objects that  
 693 gain energy from SRP after ejection can raise their periapsis to a point above the sur-  
 694 face within the first revolution. This happens most readily when the velocity at apoap-  
 695 sis is oriented away from the Sun. Thus, in addition to the magnitude of the velocity,  
 696 the orientation of the osculating orbital ellipse at ejection can be a deciding factor for  
 697 a particle's fate.

698 Fig. 7 depicts the distribution of ejection velocities, with color coding to indicate  
 699 the orbital type. Inertial or orbital velocities, which are relative to Bennu in a non-rotating  
 700 frame, predominantly range from 10–22 cm/s and show a sharp transition in orbital type  
 701 around 18–20 cm/s, corresponding to the Bennu escape velocity. The sharp drop above  
 702 the escape velocity presumably reflects a selection effect against particles that do not stay  
 703 near Bennu for long and therefore are less likely to be observed. In contrast to the in-  
 704 ertial velocities, surface-relative velocities are smeared by the velocity of the surface ( $\sim 10$   
 705 cm/s at the equator), and thus they range from 4–28 cm/s and show no sharp transi-  
 706 tion at the surface escape velocity.

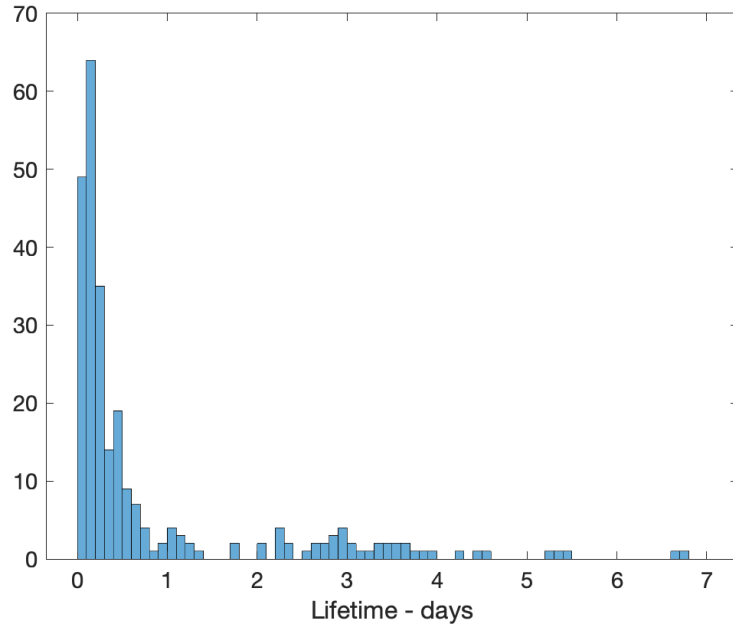


**Figure 6.** Distribution of particle lifetimes for the 259 particles having both an ejection and impact within 7 days of the mean of the observation times.

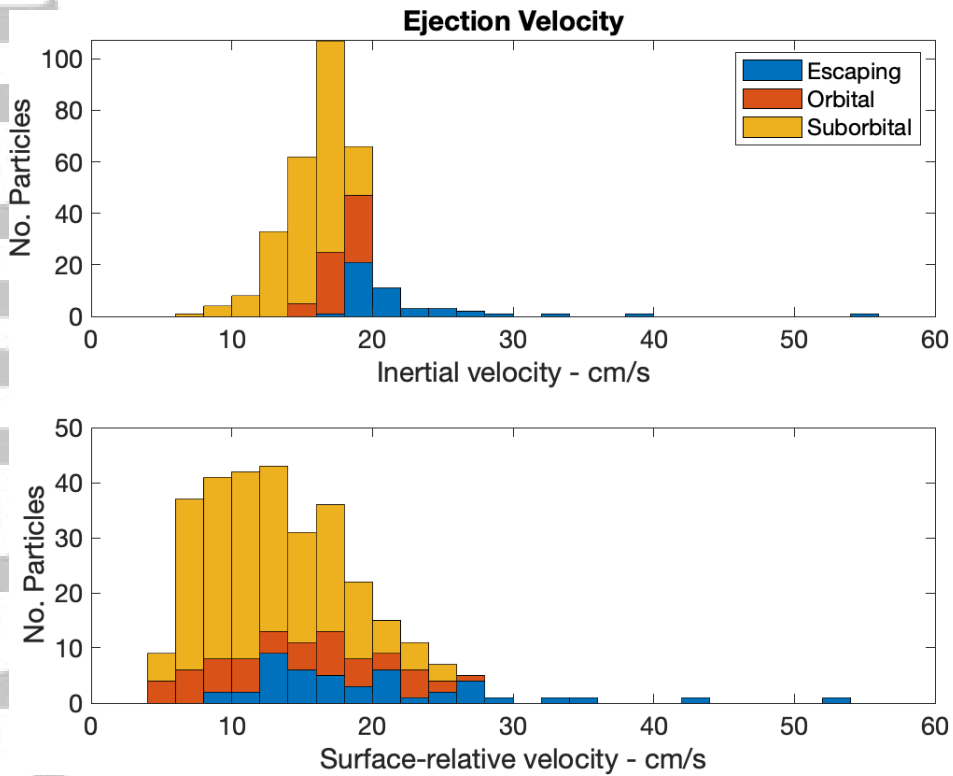


**Figure 7.** Velocity magnitude at ejection. Upper panel: orbital velocity. Lower panel: surface-relative velocity. Color coding is according to orbital type.

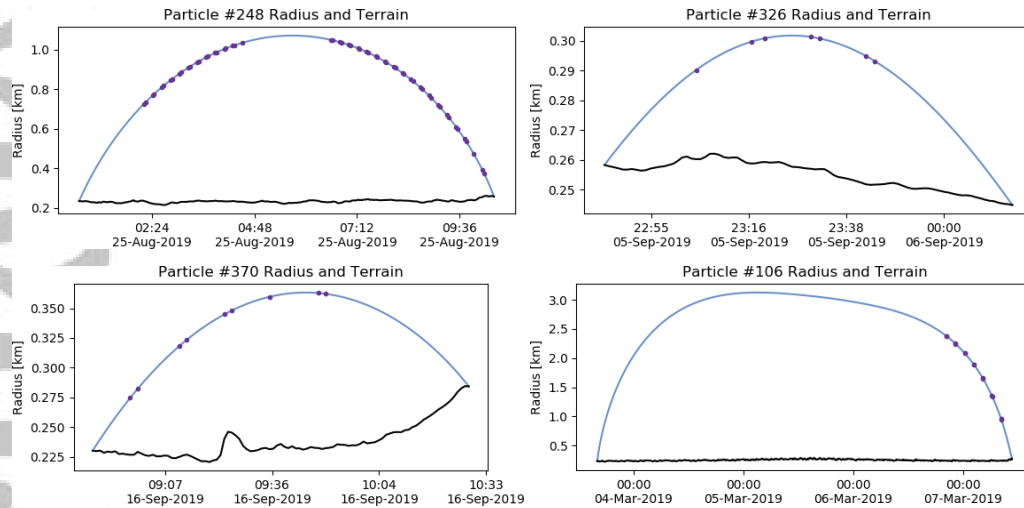


**Figure 8.** Examples of suborbital trajectories. The blue curves depict the orbital radius of the particle as a function of time, with dots marking the times of observations. The black curves represent the terrain, i.e., the radius of Bennu at the sub-particle point.

707

### 5.1.1 Suborbital particles

708

709

710

711

712

713

714

About two thirds (204/313) of our particles have suborbital trajectories, meaning that they do not survive their first periapsis passage. The apoapsis radius ranges from  $\sim 275$  m (only  $\sim 40$  m above the surface) to  $>2.5$  km, and the lifetimes range from 0.5 to 26 h. P106 is an outlier with a maximum radius  $>3$  km and lifetime of 90 h; however, the long life and relatively short data arc ( $\sim 12$  h) situated near impact leave high uncertainty as to the actual trajectory early in P106's life. Figure 8 depicts examples of suborbital trajectories, including that of P106.

715

### 5.1.2 Orbital particles

716

717

718

719

720

721

722

723

724

725

726

One fifth (63/313) of cases are quasi-elliptical orbits with more than one revolution around Bennu. Figure 9 depicts examples of orbital trajectories. This category can have as few as two revolutions, and in a few cases upwards of 10, with P2 having the most at 16 revolutions (Fig. 9). However, there are a number of objects that could have longer lifetimes, given that they do not contact the surface over our 14-day scan period, but orbital uncertainty dominates these cases and so we presume that most of them have much shorter lifetimes. In a number of cases, the nature of the trajectory, in particular the number of revolutions, is unknown. P192, for example, could actually be suborbital (Fig. 9) given that it has the minimum number of detections and a very low altitude at its first periapsis passage, thus demonstrating the potential for ambiguity in assigning the orbital type in near-transition cases.

727

### 5.1.3 Escaping particles

728

729

730

731

732

About one seventh (46/313) of the particle trajectories are hyperbolic with respect to Bennu. Figure 10 depicts examples of escaping trajectories. With few exceptions, these are all direct escape following ejection. One of these exceptions is P7, which may have escaped after the first periapsis passage, or may have returned for a second close periapsis passage before escape (Fig. 10). P137 (Fig. 10) was lofted as a part of the major

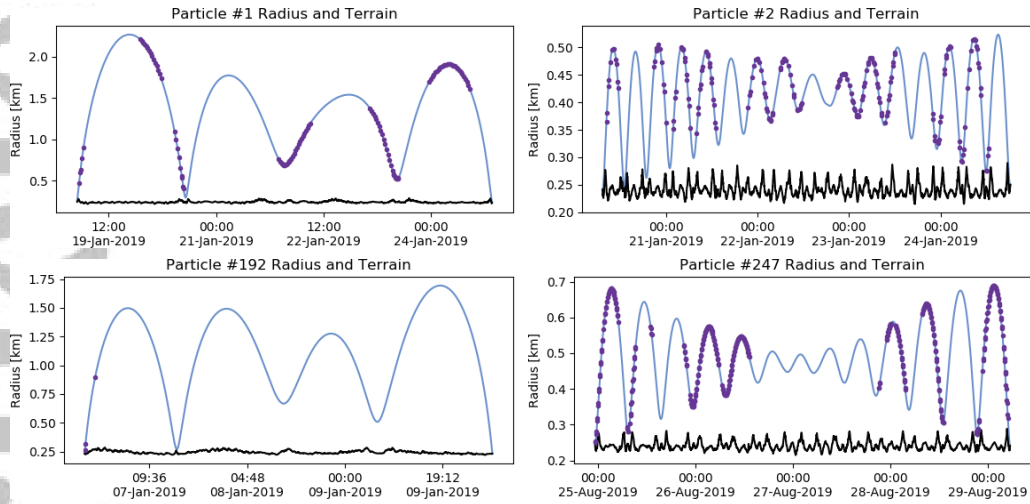


**Figure 9.** As in Fig. 8, but for orbital trajectories.

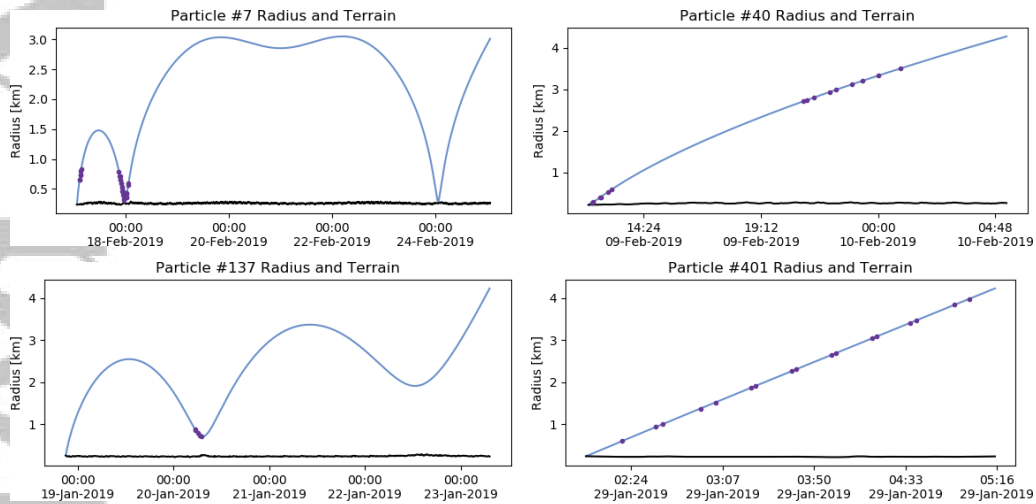


**Figure 10.** As in Fig. 8, but for escaping trajectories.

733 ejection event on 19 January 2019 and spent a few days weakly bound to Bennu before  
 734 probably being swept away by SRP.

735 **5.1.4 Hyperbolic flyby particles**

736 There is the possibility that particles could be ejected on near-parabolic or weakly  
 737 hyperbolic orbits towards the Sun, in which case SRP could slow and even reverse the  
 738 particle's escape, sending it back to the near-Bennu environment. McMahon et al. (2019  
 739 in review, this collection) have identified this type of behavior in Monte Carlo-like sim-  
 740 ulations and conclude that it can afford a very long lifetime in the Bennu environ-  
 741 ment in some cases. In this scenario, given that linking the returning particle back to its orig-  
 742 inal ejection would likely be infeasible, the particle would appear as a low-velocity hy-  
 743 perbolic flyby (or impactor). A small angle between the Sun direction and the particle's  
 744 inbound asymptote should be diagnostic of this type of trajectory. We have not seen such

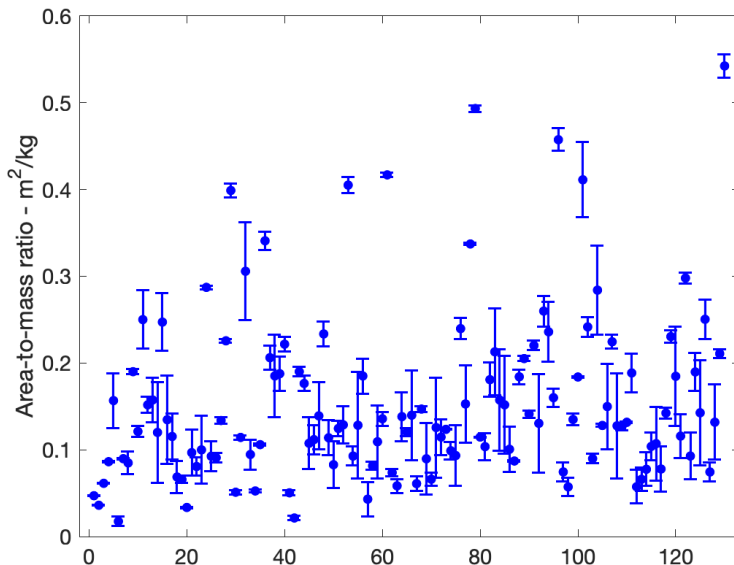


**Figure 11.** Area-to-mass ratio ( $\eta$ ) for 130 particles with well-constrained estimates.

745 cases in the solutions to date, which is not particularly surprising given that the anal-  
 746 ysis by McMahon et al. (2019 in review, this collection) found only 0.05% of their escap-  
 747 ing samples were returned to within 5 km of Bennu. With our smaller sample size, we  
 748 would not expect to see any such cases. Although our initial sampling of 390 particles  
 749 included a number of nominally hyperbolic flybys at speeds below 0.5 m/s, we are doubt-  
 750 ful that any of them are credible. Many are likely associated with a direct ejection, given  
 751 that the orbital uncertainty readily puts the particles below the surface at periastris, and  
 752 the inbound asymptotes are not oriented such that SRP would account for the returns.  
 753 Some others are likely errant solutions in a local minimum given that the Sun is not sit-  
 754 uated in a direction to explain a hyperbolic flyby. We treat all such cases as spurious and  
 755 neglect them in our analysis.

## 756 5.2 Particle Size

757 The radiation pressure acting on the particles has a significant effect on the tra-  
 758 jectories, so much so that the area-to-mass ratio  $\eta$  can be estimated with good precision.  
 759 Again, we are only able to estimate the combined direct and reflected radiation pressure  
 760 term  $\eta' = (1 + \frac{4}{9}\mathcal{A}_{\text{Bond}})\eta$ , where we assume  $\mathcal{A}_{\text{Bond}} = 0.016$  to derive  $\eta$ . The estimated  
 761 values of  $\eta$  and the associated formal uncertainties  $\sigma_\eta$  are available in our catalog (Chesley  
 762 et al., 2019). For the purposes of our discussion here, we limit the analysis to particles  
 763 for which the *a posteriori* uncertainty  $\sigma_\eta$  is not substantially controlled by our *a priori*  
 764 uncertainty constraint of  $\sigma_{\eta_{\text{prior}}} = 0.08 \text{ m}^2/\text{kg}$ . Thus we require  $\sigma_\eta < 0.8 \sigma_{\eta_{\text{prior}}}$  to en-  
 765 sure that the result is driven by the data. We also drop those cases with low significance  
 766 estimates, ensuring that the  $\eta$  estimate has an  $\text{SNR} = \frac{|\eta|}{\sigma_\eta} > 2$ . Thus we consider 130  
 767 estimated values of  $\eta$ , which we plot in Fig. 11. Many of the estimates have very low for-  
 768 mal uncertainties; e.g., 16 cases have  $\text{SNR} > 100$ , indicating a strong effect on the tra-  
 769 jectory that is plainly evident in the observations.

770 Whatever the means of ejection, it is reasonable to assume that a non-negligible  
 771 fraction of a particle's kinetic energy is rotational in nature. If we assume that the ki-  
 772 netic energy partition allows only 10% of the kinetic energy to stem from particle rota-  
 773 tion, we still have a very rapid rotation rate,  $\sim 0.3 \text{ s}$  rotation period for a typical orbit-

ing particle in simple rotation. But simple rotation is unlikely, and thus the particles should be rapidly tumbling. The area-to-mass ratios that we quote here should be representative of mean values over a time interval many orders of magnitude longer than the rotation period.

To put these values of area-to-mass ratio into context, we translate them to diameter  $D$ . For spherical particles,

$$D_\eta = \frac{3}{2\rho\eta}.$$

We take  $\rho = 2000 \text{ kg/m}^3$  based on presumed Bennu meteorite analogs (Clark et al., 2011; Hamilton et al., 2019). This leads to a set of diameters that range over 0.13–4.1 cm with median 0.56 cm, and that can be compared with those derived from particle photometry and using similar assumptions. To this end we also define the diameter  $D_H$  derived from absolute magnitude  $H$ , again assuming spherical particles, as

$$D_H = 1329 \times 10^5 \text{ cm} \cdot \frac{10^{-H/5}}{\sqrt{pV}}.$$

Hergenrother et al. (2019 in review, this collection) shows that assuming the Bennu albedo of 4.4% leads to a discrepancy in  $D_H$  compared to  $D_\eta$ , with the absolute magnitudes pointing to larger particles than the area-to-mass ratios by a median factor  $1.5\times$ . Hergenrother et al. (2019 in review, this collection) go on to show that the discrepancy can only be reconciled by assuming a significantly larger albedo (10.5%) or a significantly lower mass density ( $1340 \text{ kg/m}^3$ ) for the particles, which they argue would be challenging to explain.

To resolve this apparent discrepancy, we drop the assumption of spherical particles and assume instead an ellipsoid of revolution having semi-axes  $a \times a \times b$ , and derive the axis ratio  $p = b/a$ . We continue with the assumption of rapidly tumbling particles and obtain the average cross-sectional area  $\bar{A} = \pi a^2 f(p)$ , where the function  $f(p)$  is defined and derived in Appendix A. With this then

$$\eta = \frac{\bar{A}}{M} = \frac{3pf(p)}{4\rho a} \Rightarrow a = \frac{3pf(p)}{4\rho\eta}. \quad (1)$$

On the other hand, the photometric estimate of the size is purely dependent on the cross-section and so

$$\bar{A} = \frac{\pi}{4} D_H^2 \Rightarrow a = \frac{D_H}{2\sqrt{f(p)}}. \quad (2)$$

By combining Eq. 1 and Eq. 2, we can simultaneously determine the semimajor axis and the axis ratio of the particle, given an estimated area-to-mass ratio and absolute magnitude and assumed albedo and density. We can generally find two solutions: one corresponding to  $p < 1$ , i.e., an oblate shape, and one for  $p > 1$ , i.e., a prolate shape. We selected the former, which would imply a flake-like shape for the particles, consistent with the shapes of fragments seen in laboratory impact experiments (e.g., Capaccioni et al., 1984; Michikami et al., 2016). Figure 12 shows the resulting values of  $p$  for  $\mathcal{A} = 4.4\%$  and  $\rho = 2000 \text{ kg/m}^3$ . the distribution has a range from 0.07–1.0 and median 0.27. These results are in rough agreement with laboratory impact experiments, which tend to find axis ratios ranging from 0.2–1 with median  $\sim 0.5$  for catastrophically disrupting impacts (Capaccioni et al., 1984). However, Michikami et al. (2016) find that sub-catastrophic disruption impacts lead to lower axis ratios, with the ratio of the smallest to largest axes of fragments being as small as 0.2 in the mean, very much in accord with our distribution. If there is a discrepancy between our distribution of  $p$  and those found from impact experiments it may be a manifestation of measurement or modeling errors, but with so many samples at hand it could as well be an indication that our particles are not exclusively created by hypervelocity impacts.



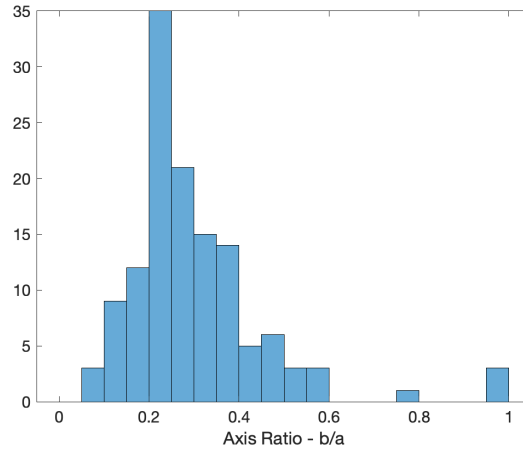


**Figure 12.** For 126 particles having reliable area-to-mass ratios and absolute magnitude estimates, the distribution of estimated particle axis ratios  $b/a < 1$  for oblate ellipsoids of revolution based on estimated area-to-mass ratios and absolute magnitudes (Hergenrother et al., 2019 in review, this collection), assuming  $\mathcal{A} = 4.4\%$  and  $\rho = 2000 \text{ kg/m}^3$

815 Some of the extreme values for the axis ratio  $p$  could be caused by the simplify-  
 816 ing assumptions in our derivations. Instead of a uniformly distributed orientation of the  
 817 particle, we could have a flake that is experiencing only a moderate wobbling, and in that  
 818 case the spacecraft might see mostly the face of the particle while the Sun might see mostly  
 819 the edge of the particle (or vice versa). This scenario would violate our averaging assump-  
 820 tions and would imply a less extreme axis ratio. Moreover, some of the outliers could  
 821 be simply explained by the formal uncertainties in  $\eta$  and  $H$ . The key point here is that  
 822 accounting for a non-spherical shape can lead to consistent size estimates from photom-  
 823 etry and SRP solutions.

824 Figure 13 plots the distribution of diameters for volume-equivalent spheres  $D =$   
 825  $2a\sqrt[3]{p}$ , which has a range 0.22–6.1 cm with median 0.74 cm, somewhat larger than the  
 826 distribution for  $D_\eta$ .

827 One candidate mechanism for driving particle ejection from the asteroid surface  
 828 is fatigue from diurnal thermal cycling (Lauretta et al., 2019; Molaro et al., 2019 in re-  
 829 view, this collection). Fatigue-driven exfoliation, the flaking of thin layers of material from  
 830 boulder surfaces, is observed widely across Bennu (Lauretta et al., 2019) and known to  
 831 drive the mobilization of disaggregated rock fragments in terrestrial environments (Collins  
 832 et al., 2018). Molaro et al. (2019 in review, this collection) developed a model to pre-  
 833 dict the characteristic spacing of exfoliation cracks in Bennu’s boulders and quantify the  
 834 particle sizes and ejection speeds that may result from an exfoliation event. The model  
 835 assumes that surface-normal exfoliation layers are disaggregated into equal-sized cubes,  
 836 each the size of the layer thickness. Here, however, we assume that the exfoliation layer  
 837 is decomposed into flakes of thickness  $2b$  with axis ratio  $p = b/a$  distributed accord-  
 838 ing to Fig. 12. This allows a range of particle sizes and volume-equivalent spherical di-  
 839 ameters. With these assumptions, Fig. 13 compares the size distribution of our partic-  
 840 les with that produced by exfoliation layers in a 1-meter boulder (Molaro et al., 2019  
 841 in review, this collection). Although the mass that may be ejected during a given exfo-  
 842 liation event is not well constrained, the shape and peak diameter of the size distribu-  
 843 tion of thermally-fractured fragments provides a good match to our results. This rein-  
 844 forces the hypothesis that particles ejected from Bennu are fragments arising from di-  
 845 urnal thermal cycling on the surface.

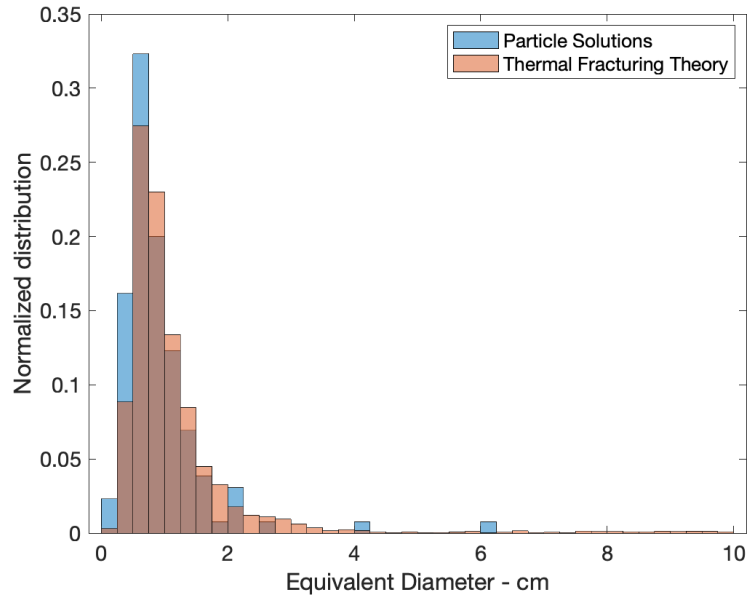


**Figure 13.** Distribution of volume-equivalent spherical diameters for our particle solutions (blue bars) based on the combined information from absolute magnitude (Hergenrother et al., 2019 in review, this collection) and area-to-mass ratio, and assuming  $\mathcal{A} = 4.4\%$  and  $\rho = 2000 \text{ kg/m}^3$ . For comparison, the plot also depicts the size distribution of thermally fractured fragments (red bars) as described in the text according to the exfoliation model by Molaro et al. (2019 in review, this collection).

846

### 5.3 Concurrent ejection events

847

848

849

850

851

852

853

854

855

856

857

858

859

860

861

We scanned our particle catalog for particles that were ejected at nearly the same time and location, which represent *ejection events*. Our orbit estimation approach is complementary to, but independent of, other event analyses, some of which are generally more robust with few detections. For example, Pelgrift et al. (2019 in review, this collection) applied kinematic constraints and detailed image processing to characterize ejection events on 6 January, 19 January, and 11 February 2019, among others. In a related effort, Leonard et al. (2019 in review, this collection) fitted dynamical orbits with the constraint that all particles in a given event were ejected at a common time and location, which could be estimated. For the present work, we do not enforce the notion that particles from ejection events emanate from a single surface location during the orbit estimation process. Rather, we use the similarity of ejection circumstances to identify candidates that may be associated with an event. After selecting a set of candidates, outliers from the weighted mean are culled (at  $>2$ -sigma) until reaching a final set. Table 2 lists the cases for which at least two particles are consistent with a common ejection. Figure 14 depicts the individual particle ejection estimates along with the weighted mean of each case.

862

863

864

865

866

867

868

869

Two of our events (19 January and 11 February) were previously characterized by Lauretta et al. (2019). In both cases, results compare reasonably well, though the ejection latitudes for the 11 February event differ by  $5^\circ$ , well outside stated uncertainties. As indicated in Fig. 14, some particles from the 11 February event have large latitude uncertainty, though some are much better constrained. We note again that our ejection uncertainty estimates are based on the formal covariance and do not account for surface topography. As seen in the following section for P57 and P58, this simplified uncertainty approach can be reasonably accurate for ejections with steeper trajectories (i.e., high el-

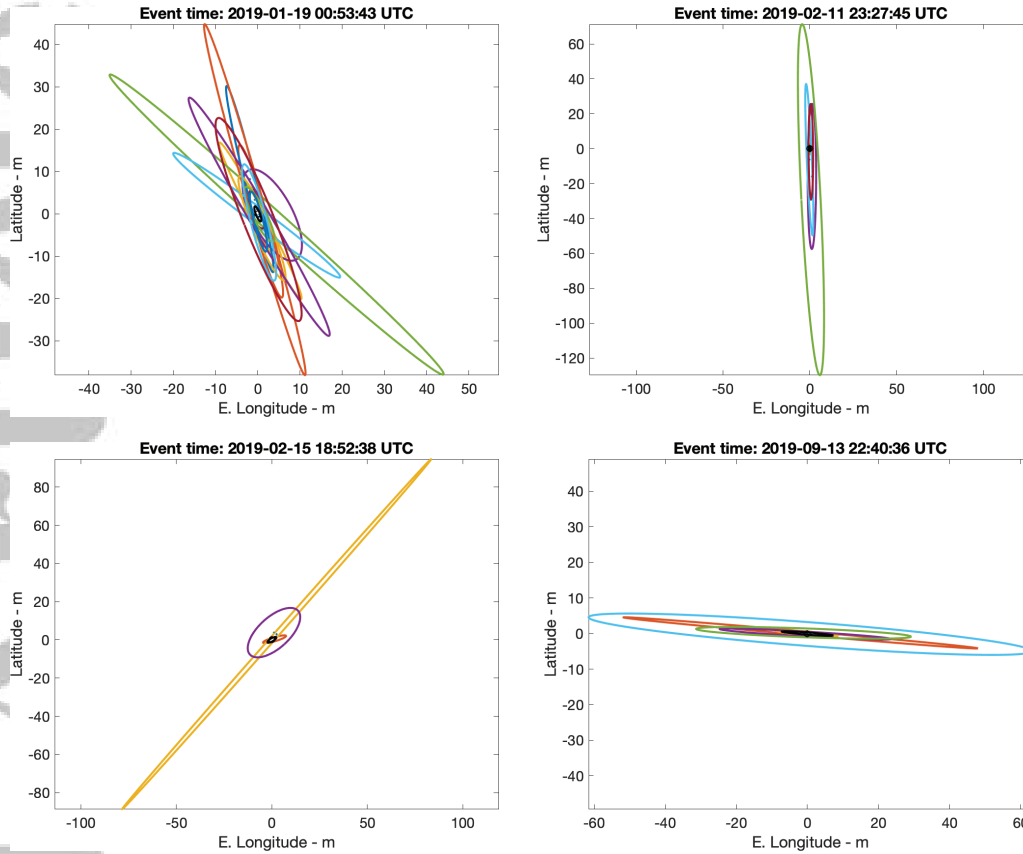


**Figure 14.** Ejection location estimates for the four events for which we have associated three or more particles (Table 2). In each case the black ellipse represents the weighted mean and uncertainty of the individual particle ejection estimates, while the colored ellipses depict the location and uncertainty of the individual particle ejection estimates. All ellipses indicate the 3-sigma confidence region.

870 evaluation angle velocity), whereas the location and probability distribution for shallower  
 871 ejections depend heavily on the local topography. The implication is that the uncertain-  
 872 ties given in Table 2 may in some cases be optimistic.

#### 873 5.4 Ejections spawned by impacts

874 On 13 February 2019, a particle was observed ricocheting off of Bennu’s surface.  
 875 During our analysis we were purposefully monitoring for such a possibility, and as a re-  
 876 sult we found that the impact time and location of P57 was suspiciously close to the ejection  
 877 time and location of P58. The location of the contact was on the dark side of Bennu  
 878 at local solar time of  $\sim 00:30$ , and took place about an hour after the last image of P57  
 879 was taken and about an hour before the first image of P58 was taken. Their nominal im-  
 880 pact and ejection locations were separated by  $\sim 15$  m on the surface and  $\sim 3$  minutes in  
 881 time, which corresponded to a 3-dimensional Mahalanobis distance of  $\sim 6$  sigma when  
 882 using the mapped covariances output from the OD process.

883 However, we suspected the formal OD uncertainties to be optimistic, in which case  
 884 the statistical agreement would potentially be much greater. In particular, the timing

## Accepted Article

**Table 2.** Summary of candidate event times, locations and local solar times (LST). Location is given in degrees of longitude and latitude, while the associated uncertainties are tabulated in meters to better convey the scale of the spatial uncertainty. The number of particles  $N_{\text{part}}$  used in the estimate and the catalog numbers of the associated particles are also listed.

Time (UTC)	Longitude	Latitude	LST	$N_{\text{part}}$	Particle Numbers
2019-01-19 00:53:43 $\pm$ 3 s	335.383° $\pm$ 0.4 m	19.925° $\pm$ 0.9 m	16:39:41	14	126 127 129 135 136 173 174 176 182 183 196 200 202 203
2019-01-26 09:26:55 $\pm$ 61 s	11.369° $\pm$ 1.4 m	-25.004° $\pm$ 3.0 m	22:00:25	2	175 181
2019-02-11 23:27:45 $\pm$ 4 s	59.739° $\pm$ 0.3 m	15.065° $\pm$ 0.7 m	18:06:50	6	51 54 162 165 167 169
2019-02-15 18:52:38 $\pm$ 20 s	55.707° $\pm$ 1.1 m	8.017° $\pm$ 0.7 m	00:50:13	3	80 83 84
2019-08-16 10:51:59 $\pm$ 74 s	248.834° $\pm$ 1.5 m	32.606° $\pm$ 2.6 m	20:12:26	2	29 228
2019-08-23 10:36:57 $\pm$ 33 s	196.423° $\pm$ 1.1 m	48.741° $\pm$ 10.0 m	18:07:17	2	315 316
2019-08-28 18:35:28 $\pm$ 195 s	74.046° $\pm$ 11.6 m	42.728° $\pm$ 17.0 m	05:06:20	2	263 267
2019-09-05 22:44:34 $\pm$ 33 s	319.315° $\pm$ 2.3 m	-10.689° $\pm$ 3.9 m	13:34:56	2	326 327
2019-09-13 22:40:36 $\pm$ 4 s	20.595° $\pm$ 1.5 m	-65.379° $\pm$ 0.3 m	10:13:26	5	343 344 345 353 354
2019-09-14 04:25:25 $\pm$ 25 s	181.255° $\pm$ 1.2 m	32.266° $\pm$ 1.8 m	05:03:00	2	359 360

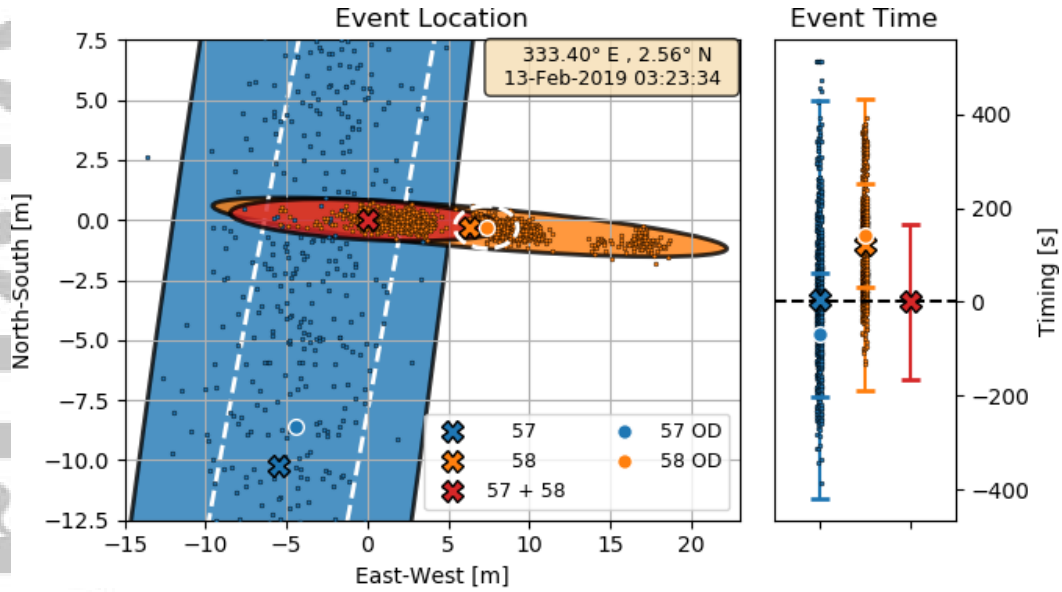


**Figure 15.** Bounce footprint (left) and timing (right), demonstrating agreement between the impact of P57 and ejection of P58. The blue and orange dots denote the propagated Monte Carlo samples. The blue and orange ellipses (errors) are 3 sigma and are computed from the empirical covariances of the samples. The crosses indicate their respective means, and the joint solution is shown in red. The timing is centered about the joint solution. The formal OD solutions are shown in white.

885 and along-track uncertainties did not fully account for Bennu's terrain, which is extremely  
 886 rugged. This is a potentially large and nonlinear source of additional uncertainty that  
 887 will preferentially affect trajectories that intersect at shallow elevation angles. This led  
 888 us to conduct a Monte Carlo analysis in an attempt to capture the full nonlinear uncer-  
 889 tainty. For both P57 and P58, the correlated estimated covariances were sampled 1000  
 890 times at the filter epoch (the mid-time of their respective observations), and each sam-  
 891 ple was propagated to the surface. The results are shown in Fig. 15. The primary driver  
 892 in the difference in uncertainty between the P57 and P58 solutions is the difference in  
 893 number of observations: P57 appeared in 7 images and P58 appeared in 24 images.

894 The first obvious trend to point out is the markedly non-Gaussian nature of P58's  
 895 samples. P58 departs at a fairly shallow angle of  $\sim 20^\circ$ , meaning that trajectory errors  
 896 consistent within the formal uncertainties will lead to surface intersections at different  
 897 points that appear outside of the uncertainty because the samples will collide with dif-  
 898 ferent rocks or features. This leads to three groupings in the possible ejection point spread  
 899 out in the along-track direction. P57, on the other hand, impacts at a much steeper an-  
 900 gle of  $\sim 67^\circ$ . Consequently, the formal OD covariance much more accurately captures the  
 901 Monte Carlo dispersions because the shape intersection is less sensitive to the topogra-  
 902 phy. In terms of Fig. 15, P57's along-track error is roughly normal to the page on the  
 903 left plot and appears primarily as the timing uncertainty in the right plot.

904 The dispersions in Fig. 15 alone are not enough to claim that P57 and P58 are in  
 905 fact the same object. It is also vitally important to check that the inbound and outbound  
 906 orbital velocities are dynamically consistent. In Bennu's rotating frame, we would ex-  
 907 pect the magnitude of the outbound velocity to be smaller than the magnitude of the  
 908 inbound velocity, and for the change in direction to make sense physically. In other words,

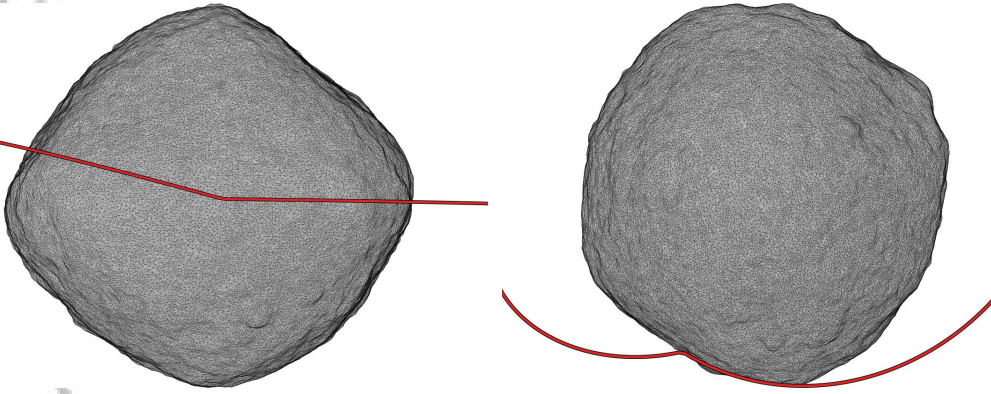


**Figure 16.** Orbital diagrams of the ricocheting particle. The left view is from directly above the event location at  $333^\circ$  E and  $2.5^\circ$  N, and the right view is from above Bennu's north (+z) pole. The shape is rendered at the event time. The plotted trajectories span 2 hours in total, centered on the bounce time. The trajectory is traversing from left to right in both views, and Bennu's pole is pointing up on the left and towards the viewer on the right.

909 we would expect to find a coefficient of restitution, COR,  $< 1$  and the arrival and de-  
 910 parture elevation angles to be  $> 0$ .  $COR < 1$  is a hard dynamical constraint, provided  
 911 the absence of any external forces at the moment of impact (such as fission or outgassing),  
 912 and the departure elevation condition is met trivially for both objects (otherwise they  
 913 would not impact/eject). Although the change in direction is captured implicitly in the  
 914 COR, we also performed visual inspections of the trajectories.

915 The orbits are plotted in Fig. 16. The orbits shown were hand-picked from the set  
 916 of Monte Carlo samples in Fig. 15 to be near the joint solution (discussed later in this  
 917 section) so they appear continuous in both space and time. The most powerful way to  
 918 view this is via animation (see Chesley et al., 2019), which captures the relative veloc-  
 919 ities of the orbits and Bennu's surface. Even so, Fig. 16 tells the tale quite well when com-  
 920 bined with the ricochet statistics in Table 3. When inspecting the inbound and outbound  
 921 velocities in Bennu's rotating frame, we find that the outbound velocity is in fact smaller  
 922 than the inbound, yielding a COR estimate of  $\sim 0.57$ . This value assumes that the event  
 923 was a single bounce (rather than impact, roll, relaunch, or multiple bounces), and we  
 924 are unable to say with certainty whether any mass was lost during impact. The inertial  
 925 velocities also tell an interesting story, namely that the departing velocity is higher than  
 926 the arrival velocity. This is because Bennu's surface is traveling faster in inertial space  
 927 than the velocity of the inbound particle, meaning that Bennu literally kicks the par-  
 928 ticle back into orbit. This effect is enhanced by the fact that the bounce point is near  
 929 the equator, where Bennu's surface speed is greatest. As a result, the collision reduces  
 930 the inclination from  $17^\circ$  to  $3^\circ$ , meaning that the post-bounce velocity vector is indeed  
 931 strongly aligned with Bennu's surface velocity, consistent with the idea that Bennu kicked  
 932 the object back into orbit. The bounce results in a net energy transfer from Bennu to  
 933 the particle of  $\sim 2.7$  mJ/kg, shown graphically in Fig. 17. Taken together, the energy trans-  
 934 fer leads to an orbit with increased semimajor axis, reduced eccentricity, and reduced  
 935 inclination (Table 3.) This illustrates the fascinatingly complex dynamical environment  
 936 around small bodies.

937 Now, based on the dispersions in Fig. 15 and the dynamical feasibility shown in  
 938 Table 3, we can say with high confidence that P57 and P58 are the same object. This  
 939 conclusion is reinforced by the agreement in absolute magnitude (Table 3) for the two

**Table 3.** Detailed information on the orbital and physical characteristics of P57 and P58, as well as the circumstances of the associated bounce.

Parameter	P57	P58
Propagation time ( $ t_{\text{filter}} - t_{\text{event}} $ )	91 min	93 min
Number of observations	7	24
Area-to-mass ratio	$0.09 \pm 0.09$	$0.053 \pm 0.003$
Absolute magnitude <sup>‡</sup>	$42.82 \pm 0.44$	$42.35 \pm 0.5$
Orbital inclination <sup>†</sup>	17°	3°
Orbital semi-major axis <sup>†</sup>	0.25 km	0.41 km
Orbital eccentricity <sup>†</sup>	0.62	0.29
Inbound/outbound elevation	67°	20°
Inbound/outbound velocity mag. (body frame)	9.48 cm/s	5.48 cm/s
Inbound/outbound velocity mag. (inertial)	14.03 cm/s	15.89 cm/s
Bounce epoch	2019-02-13 03:23:34 ET $\pm$ 55 s	
Bounce longitude	$333.4^\circ \pm 0.6^\circ$	
Bounce latitude	$2.6^\circ \pm 0.1^\circ$	
Bounce local solar time	00:22:35 $\pm$ 340 s	
Change in kinetic energy	$+2.68 \pm 0.16$ mJ/kg	
Coefficient of Restitution*	$0.57 \pm 0.01$	

Notes: <sup>‡</sup>(Hergenrother et al., 2019 in review, this collection) <sup>†</sup>Based on osculating orbit at filter epoch. \*Assuming single bounce, no mass loss.

940 particles reported by Hergenrother et al. (2019 in review, this collection). The P57 tra-  
 941 jectory fit provides no information on area-to-mass ratio, but that of P58 has SNR  $\sim$   
 942 20 and, together with the absolute magnitude, indicates an equivalent diameter 1.9 cm.

943 Finally, we compute a joint estimate of the bounce location and time. Initially we  
 944 computed this linearly using the empirical means and covariances of the Monte Carlo  
 945 samples by solving the normal equations associated with them. This produced a believ-  
 946 able estimate, but this method did not account for the non-Gaussian nature of P58. In  
 947 order to produce a less biased estimate we calculated the weighted mean and covariance  
 948 of P58's samples, where the samples were weighted by their distance from P57's solu-  
 949 tion. We leveraged the fact that P57's Monte Carlo dispersions appeared Gaussian which  
 950 allowed us to use P57's empirical mean and covariance to weight P58's samples. This  
 951 yielded the joint solution shown in Figure 15. We note that this joint solution falls on  
 952 a bouldery area of Bennu's surface that is substantially devoid of fine material, which  
 953 is consistent with the nature of a ricochet. A complete analysis of the bounce in light  
 954 of the detailed topography of the area could isolate specific locations in the joint solu-  
 955 tion footprint that are consistent with the pre- and post-bounce trajectories.

## 956 5.5 General Characteristics of Ejections and Impacts

957 We have so far identified several simultaneous ejection events, and described a case  
 958 where an ejection is linked directly to a concurrent impact. Now we turn to an exam-  
 959 ination of the properties of ejections and impacts in a broad sense. We limit the discus-  
 960 sion here to those impacts and ejections having no more than 15° uncertainty in the lat-  
 961 itude and longitude of the location. This limitation leaves 181 ejections and 166 impacts  
 962 to be analyzed.

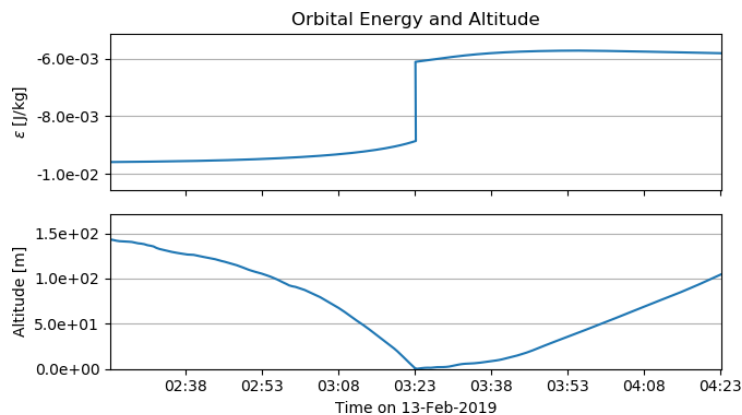


**Figure 17.** Specific orbital energy (top) and altitude (bottom) of P57 before the bounce and P58 after.

963 Figure 18 depicts the distribution of Bennu local solar time (LST) at the time and  
 964 location of each ejection and impact. There is a clear enhancement of ejections during  
 965 the afternoon and especially the evening on Bennu, even while there is a background of  
 966 ejections taking place at all times of day. This is true both for the concentrated ejection  
 967 events from Table 2 and the *sporadic* ejections that are so far not tied to an event. The  
 968 LST for impacts appears more randomized, though there remains a slight enhancement  
 969 of evening impacts. This may be a random fluctuation; however, suborbital trajectories  
 970 that almost survive their first periapsis passage would tend to impact at an LST sim-  
 971 ilar to that of their ejection, while others would be randomized. Thus the slight enhance-  
 972 ment in evening impacts could be related to that seen for ejections.

973 The afternoon/evening ejection enhancement is consistent with two hypotheses for  
 974 ejection. Molaro et al. (2019 in review, this collection) find that the diurnal thermal cycle  
 975 has peak thermal stresses in the afternoon when maximum temperatures occur and  
 976 then after nightfall due to rapid cooling. This leads them predict that ejections due to  
 977 thermal fatigue would occur during this time. On the other hand, given Bennu’s retro-  
 978 grade rotation, the afternoon and evening ejections arise from Bennu’s forward-facing  
 979 hemisphere, as defined by its heliocentric orbit. This is in line with predictions that me-  
 980 teoroid impacts will predominate on the leading hemisphere (Bottke et al., 2019 in re-  
 981 view, this collection). And yet our results do show a far more significant background of  
 982 ejections on the morning hemisphere than is predicted by either model. We speculate  
 983 that this is due to ejections caused by particle impacts, which has been demonstrated  
 984 above for P57 and P58.

985 Figure 19 depicts the distribution of the sine of latitude for ejections and impacts,  
 986 which should be uniform for an area-wise uniform distribution on a sphere. We separate  
 987 the related ejection events from the sporadic (singleton) ejections in the plot in order to  
 988 discern any significant differences between the two, though none is apparent. The 19 Jan-  
 989 uary event, with 14 associated ejections, dominates the distribution of events. Both ejec-  
 990 tions and impacts show an excess in the equatorial regions and are more sparse at the  
 991 poles. For impacts, the equatorial excess is more pronounced and is not unexpected, given  
 992 the fact that the equatorial region has the highest radius terrain, and so a decaying or-  
 993 bit is more likely to intersect with the surface in this region. For the ejections, we note  
 994 that Bottke et al. (2019 in review, this collection) predicts an excess of meteoroid im-  
 995 pacts in the equatorial region, which is primarily a manifestation of lower projected ar-  
 996 eas onto the meteoroid impact plane in the polar regions. In contrast, Molaro et al. (2019



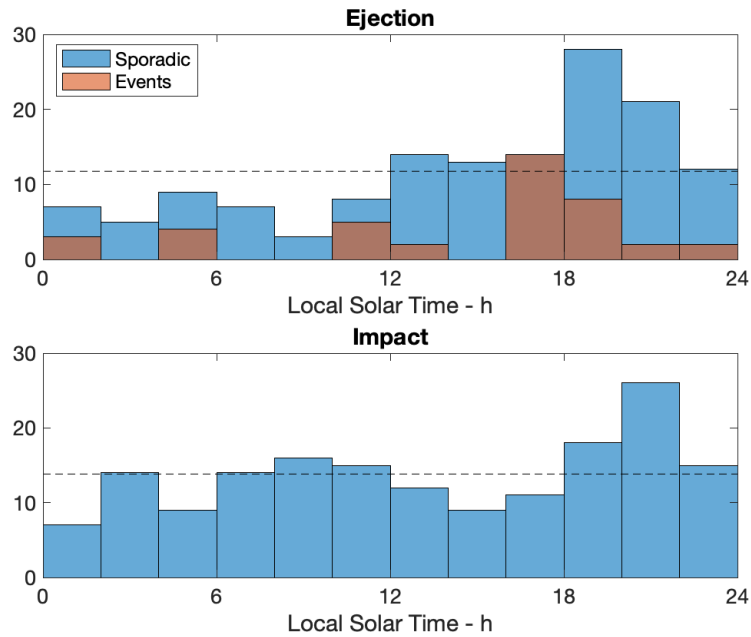


**Figure 18.** Distribution of local solar time (LST) at ejection (upper panel) and impact (lower panel). For ejections, we plot the histogram of ejections associated with events separate from singleton ejections, which we term sporadic. As reference, the dashed line marks the uniform distribution, given the total number of sporadic ejections (top) and impacts (bottom).

997 in review, this collection) do not predict a deviation from uniform latitudinal distribu-  
 998 tion.

## 999 5.6 Gravity estimate

1000 We derived a particle-based gravitational field, truncated at degree and order 10,  
 1001 by simultaneously estimating the gravitational field for a number of well-observed par-  
 1002 ticles. This served the dual purposes of constraining the gravitational field of Bennu for  
 1003 follow-on geophysical studies and facilitating more reliable orbit estimation for the many  
 1004 particles that did not have a solid gravitational signal, i.e., those having few detections  
 1005 or short data arcs or both. The ongoing radio science investigation of the OSIRIS-REx  
 1006 spacecraft motion about Bennu will yield an independent estimate of Bennu’s gravity  
 1007 field. These separate approaches, from spacecraft and particles, will be compared and  
 1008 unified in a forthcoming report, which will also consider the geophysics implications of  
 1009 Bennu’s gravity field.

1010 For this effort, we selected those particles with more than 30 detections and hav-  
 1011 ing observational arcs either more than 6 h in length or covering more than 80% of the  
 1012 particle lifetime. The latter constraint allowed well-observed sub-orbital particles to be  
 1013 included in the gravity estimate. This led to a set of 20 particles, which are listed in Ta-  
 1014 ble 4, along with their relevant particulars such as arc length and number of detections.

1015 The *a priori* values for the harmonic coefficients come directly from shape model  
 1016 integration, assuming constant density. We used the modified Kaula rule for Bennu to  
 1017 generate the *a priori* uncertainties (McMahon et al., 2018). Degree 1 terms, reflective  
 1018 of offsets between the center of mass and center of volume, were zeroed and not estimated.  
 1019 Based on higher-fidelity modeling from optical imaging, we enforced the assumption that

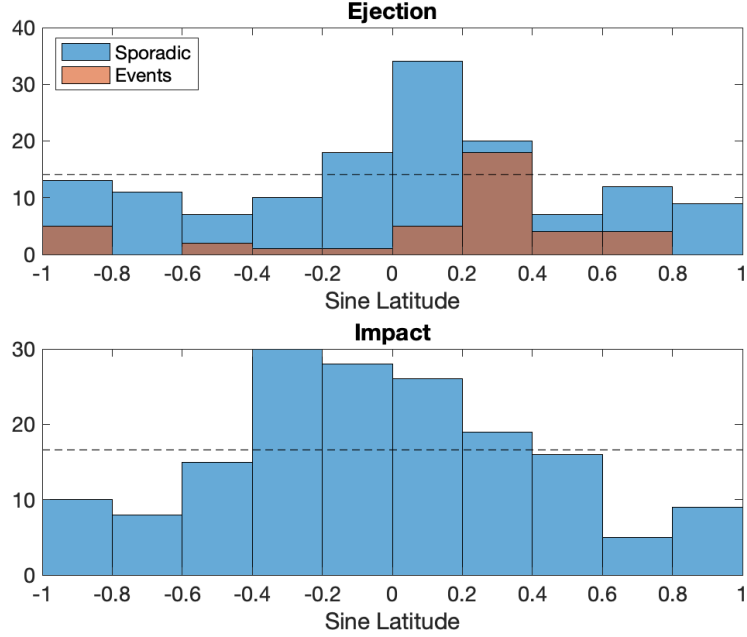


**Figure 19.** Latitudinal distribution of ejections (upper panel) and impacts (lower panel). As in Fig. 18, we plot the sporadic and event-related ejections separately, and the dashed line marks the uniform distributions (sporadic for ejections), which here correspond to a uniform area-wise distribution on a sphere.

1020 Benu is in simple rotation, and thus the  $C_{2,1}$  and  $S_{2,1}$  terms were zeroed and not es-  
 1021 timated. When estimating the gravity field we did estimate the rotation axis orienta-  
 1022 tion, with *a priori* constraints from spacecraft radio science, but the particle tracking  
 1023 data are not strongly sensitive to spin axis orientation, and there was no appreciable de-  
 1024 viation from the *a priori* values.

1025 This 20-particle joint gravity estimate yielded Benu’s gravitational parameter,  $GM =$   
 1026  $4.8904 \pm 0.0009 \text{ m}^3/\text{s}^2$ . This is consistent with the OSIRIS-REx post-rendezvous es-  
 1027 timate, which was  $GM = 4.892 \pm 0.006 \text{ m}^3/\text{s}^2$  (Scheeres et al., 2019). The spherical  
 1028 harmonic coefficients are listed in Table 5 with the full expansion through degree 5 and  
 1029 zonal terms through degree 10. The coefficients of the spherical harmonic expansion were  
 1030 well determined through degree 4, where all but two of the 19 coefficients through de-  
 1031 gree and order 4 have  $\text{SNR} > 3$ . The full gravitational field with covariance is avail-  
 1032 able from Chesley et al. (2019)

1033 Figure 20 indicates the difference at each degree between our estimate and the shape-  
 1034 based (i.e., uniform density) field, along with the RMS uncertainty at each degree. From  
 1035 the plot it is clear that the the particles are sensitive to gravitational harmonics through  
 1036 degree 8, though we are unable to distinguish nonuniform mass distribution beyond de-  
 1037 gree 3.

1038 Figure 21 shows the map of the radial acceleration difference between the observed  
 1039 gravity field and the gravity computed from shape (uniform-density Benu), which is of-  
 1040 ten called the Bouguer anomaly map (Park et al., 2016). The Bouguer anomaly was mapped  
 1041 to the reference sphere (i.e., 290 m radius) for spherical harmonic coefficients up to de-  
 1042 gree 6, excluding the degree 1 terms. The maximum Bouguer anomaly of  $\sim 65 \mu\text{Gal}$  is  
 1043 at longitude  $90^\circ$  and near the equator.

**Table 4.** The 20 particles used for our gravity estimate, with the number of detections  $N_{det}$ , the data arc (duration of the observed data set), and the lifetime. For reference, the approximate semimajor axis  $a$ , eccentricity  $e$  and inclination  $i$  at the mean epoch of the observations are also listed. The table is sorted by data arc in descending order. In this table, the seven cases with a lifetime shorter than a day are well-observed suborbital trajectories.

Particle No.	$N_{det}$	Data arc (d)	Lifetime (d)	$a$ (km)	$e$	$i$ (deg)
1	107	5.45	5.79	1.05	0.27	88
247	378	4.23	4.26	0.49	0.13	87
2	185	4.17	4.45	0.40	0.11	83
41	43	2.92	5.35	1.29	0.52	14
3	92	2.58	2.65	0.49	0.12	15
303	217	2.30	2.91	0.44	0.13	29
213	42	1.63	3.30	0.88	0.53	165
4	75	1.58	2.30	0.41	0.17	128
273	81	1.53	2.39	1.34	0.76	17
188	34	1.05	1.12	0.48	0.04	2
289	101	0.65	3.68	0.55	0.39	5
302	35	0.50	3.45	0.53	0.50	7
252	78	0.34	2.37	0.59	0.11	83
248	58	0.33	0.40	0.58	0.87	130
15	66	0.33	0.47	0.61	0.72	1
210	35	0.32	0.33	0.49	0.96	75
50	33	0.28	0.44	0.59	1.00	111
16	47	0.24	0.27	0.45	0.59	16
285	46	0.19	0.21	0.38	0.78	32
269	45	0.19	0.23	0.41	0.43	5

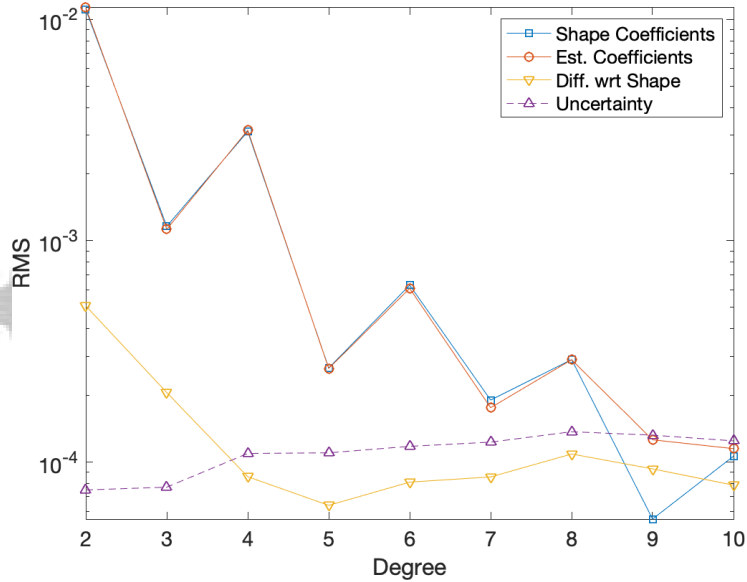


**Figure 20.** The RMS of gravitational spherical harmonic coefficients per degree. The uppermost curves depict the estimated gravity field and that obtained from the Bennu shape model assuming uniform density. The difference between these two fields is also depicted, as is the RMS of the coefficient uncertainties at each degree.

**Table 5.** Estimated spherical harmonic coefficients (normalized) with uncertainty. All coefficients are estimated through degree 10, but we tabulate sectorial and tesseral coefficients only through degree 5 and zonal coefficients through degree 10. The corresponding coefficients derived from the shape model assuming a uniform density are also tabulated, along with the relative and statistical deviations of our estimate from the uniform density assumption. The reference radius for the expansion is 290 m, and the estimated  $GM = 4.8904 \pm 0.0009 \text{ m}^3/\text{s}^2$

Coefficient	Estimated Value	Shape Value	SNR	Deviation (relative)	Deviation (sigma)
$J_2$	$1.926 \times 10^{-2} \pm 5.2 \times 10^{-5}$	$1.881 \times 10^{-2}$	370.4	0.02	8.70
$C_{2,2}$	$3.06 \times 10^{-3} \pm 5.3 \times 10^{-5}$	$3.55 \times 10^{-3}$	58.2	-0.14	-9.23
$S_{2,2}$	$-1.09 \times 10^{-3} \pm 1.1 \times 10^{-4}$	$-7.85 \times 10^{-4}$	10.3	0.39	-2.90
$J_3$	$-1.22 \times 10^{-3} \pm 7.9 \times 10^{-5}$	$-1.30 \times 10^{-3}$	15.5	-0.06	1.00
$C_{3,1}$	$8.15 \times 10^{-4} \pm 2.9 \times 10^{-5}$	$1.01 \times 10^{-3}$	28.0	-0.19	-6.66
$S_{3,1}$	$-5.43 \times 10^{-4} \pm 4.3 \times 10^{-5}$	$-3.44 \times 10^{-4}$	12.5	0.58	-4.59
$C_{3,2}$	$-9.35 \times 10^{-4} \pm 4.6 \times 10^{-5}$	$-7.25 \times 10^{-4}$	20.5	0.29	-4.61
$S_{3,2}$	$-5.38 \times 10^{-4} \pm 4.9 \times 10^{-5}$	$-7.41 \times 10^{-4}$	11.0	-0.27	4.17
$C_{3,3}$	$1.17 \times 10^{-3} \pm 6.0 \times 10^{-5}$	$1.19 \times 10^{-3}$	19.5	-0.02	-0.39
$S_{3,3}$	$-3.1 \times 10^{-4} \pm 8.3 \times 10^{-5}$	$-2.8 \times 10^{-4}$	3.7	0.13	-0.42
$J_4$	$-6.50 \times 10^{-3} \pm 7.1 \times 10^{-5}$	$-6.39 \times 10^{-3}$	91.4	0.02	-1.44
$C_{4,1}$	$-8.82 \times 10^{-4} \pm 5.8 \times 10^{-5}$	$-8.98 \times 10^{-4}$	15.3	-0.02	0.28
$S_{4,1}$	$-5.8 \times 10^{-4} \pm 6.0 \times 10^{-5}$	$-6.8 \times 10^{-4}$	9.6	-0.15	1.68
$C_{4,2}$	$-8.71 \times 10^{-4} \pm 5.5 \times 10^{-5}$	$-8.29 \times 10^{-4}$	16.0	0.05	-0.77
$S_{4,2}$	$-8.4 \times 10^{-5} \pm 6.5 \times 10^{-5}$	$-8.1 \times 10^{-5}$	1.3	0.03	-0.04
$C_{4,3}$	$-7.6 \times 10^{-5} \pm 6.8 \times 10^{-5}$	$-9.6 \times 10^{-5}$	1.1	-0.20	0.29
$S_{4,3}$	$-3.9 \times 10^{-4} \pm 6.3 \times 10^{-5}$	$-4.4 \times 10^{-4}$	6.1	-0.13	0.90
$C_{4,4}$	$7.7 \times 10^{-4} \pm 1.6 \times 10^{-4}$	$6.7 \times 10^{-4}$	4.9	0.15	0.65
$S_{4,4}$	$2.25 \times 10^{-3} \pm 8.5 \times 10^{-5}$	$2.24 \times 10^{-3}$	26.5	0.00	0.04
$J_5$	$6.7 \times 10^{-5} \pm 1.0 \times 10^{-4}$	$1.2 \times 10^{-4}$	0.7	-0.42	-0.47
$C_{5,1}$	$-3.5 \times 10^{-4} \pm 8.4 \times 10^{-5}$	$-3.5 \times 10^{-4}$	4.2	0.00	-0.00
$S_{5,1}$	$1.6 \times 10^{-4} \pm 7.9 \times 10^{-5}$	$1.7 \times 10^{-4}$	2.0	-0.03	-0.07
$C_{5,2}$	$-3.7 \times 10^{-5} \pm 8.1 \times 10^{-5}$	$1.1 \times 10^{-5}$	0.5	-4.27	-0.60
$S_{5,2}$	$-2.7 \times 10^{-4} \pm 7.4 \times 10^{-5}$	$-3.4 \times 10^{-4}$	3.6	-0.20	0.91
$C_{5,3}$	$-2.2 \times 10^{-6} \pm 8.2 \times 10^{-5}$	$-8.3 \times 10^{-6}$	0.0	-0.74	0.08
$S_{5,3}$	$-9.5 \times 10^{-6} \pm 7.5 \times 10^{-5}$	$-4.1 \times 10^{-5}$	0.1	-0.77	0.42
$C_{5,4}$	$3.2 \times 10^{-4} \pm 7.2 \times 10^{-5}$	$3.0 \times 10^{-4}$	4.5	0.08	0.34
$S_{5,4}$	$5.0 \times 10^{-5} \pm 8.2 \times 10^{-5}$	$9.9 \times 10^{-5}$	0.6	-0.49	-0.59
$C_{5,5}$	$-2.3 \times 10^{-5} \pm 8.7 \times 10^{-5}$	$4.6 \times 10^{-5}$	0.3	-1.50	-0.79
$S_{5,5}$	$3.0 \times 10^{-4} \pm 7.3 \times 10^{-5}$	$2.2 \times 10^{-4}$	4.1	0.38	1.11
$J_6$	$1.37 \times 10^{-3} \pm 8.2 \times 10^{-5}$	$1.44 \times 10^{-3}$	16.7	-0.05	-0.87
$J_7$	$-7.9 \times 10^{-5} \pm 1.2 \times 10^{-4}$	$-8.8 \times 10^{-5}$	0.7	-0.11	0.08
$J_8$	$-6.8 \times 10^{-4} \pm 1.1 \times 10^{-4}$	$-7.0 \times 10^{-4}$	6.2	-0.03	0.17
$J_9$	$-3.5 \times 10^{-5} \pm 1.0 \times 10^{-4}$	$4.2 \times 10^{-5}$	0.3	-1.84	-0.75
$J_{10}$	$2.0 \times 10^{-4} \pm 9.9 \times 10^{-5}$	$2.6 \times 10^{-4}$	2.0	-0.22	-0.59

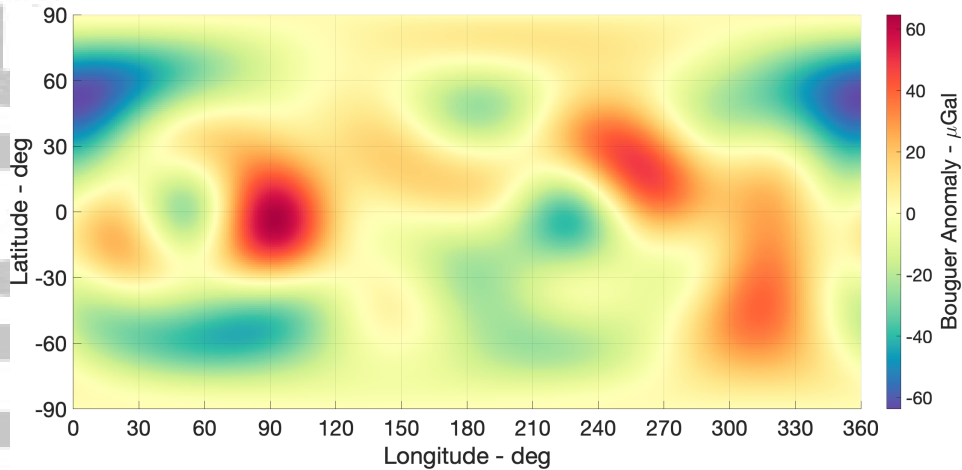


**Figure 21.** Bouguer anomaly map for Bennu’s estimated gravity field. Red-orange (green-blue) regions indicate regions of higher (lower) surface accelerations than those derived from the shape assuming uniform density.

1044

### 5.7 Interpretation of empirical accelerations

1045

1046

1047

1048

1049

1050

1051

1052

1053

In Sec. 3, we described the details of the force model that we apply to the particles. As a part of the force modeling, we estimate any unmodeled forces that are required to keep the particle on its observed trajectory. These empirical forces are in many cases negligible, but in some cases not ignorable. To demonstrate the need for empirical forces, we consider as a case study the 1.7 cm particle P1. This particle follows a roughly polar orbit (Fig. 22) with high apoapsis, mitigating some potential sources of force mismodeling, for example, gravity field, shadowing, and radiation from Bennu. Thus, while P1 is not an extraordinary case, it makes for a good example of behaviors commonly seen on particles with data arcs longer than about a half day.

1054

1055

1056

1057

1058

1059

Despite the presumably simpler dynamical model that could be appropriate for P1, we could not obtain acceptable fits even with the full, detailed dynamical model including all of the known forces listed in Table 1. Figure 23(a) depicts the postfit RA-DEC residuals from such a fit, for which we find a collective WRMS of 15.0. Not only are the residuals large, but clear trends are visible, indicating dynamical mismodeling or systematic errors in observational modeling, rather than observational noise.

1060

1061

1062

1063

1064

1065

1066

1067

1068

1069

Next we ask whether spacecraft position errors could be the cause of the large residuals, and to this end we estimate the spacecraft position error as described above in Sec. 4.2, but still not allowing for empirical accelerations. While the resulting WRMS is much lower ( $\sim 2.74$ ), it is still poor, and more importantly, much of the signature seen in Fig. 23(a) remains plainly apparent, though more muted. And even as the fit remains poor, the estimated corrections to the spacecraft trajectory are very large, as large as  $\pm 5$  m, and even extending to 10 m briefly. This is an implausible deviation from the OSIRIS-REx spacecraft ephemeris estimate, which is expected to be within a few tens of centimeters. Thus we conclude that spacecraft position errors alone cannot account for the poor residuals in Fig. 23(a).

1070

1071

1072

1073

Finally, we turn to estimating the empirical accelerations, while continuing to estimate the spacecraft position errors as before. As indicated in Fig. 23(b), the resulting postfit residuals are small (WRMS  $\sim 0.12$ ) and show no significant trends. At the same time, the estimated spacecraft position errors fell to realistic levels, with peaks in the

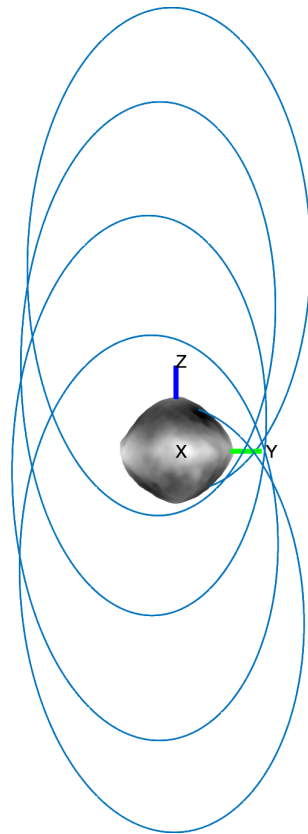


**Figure 22.** Trajectory of P1 as seen looking from the direction of the Sun.

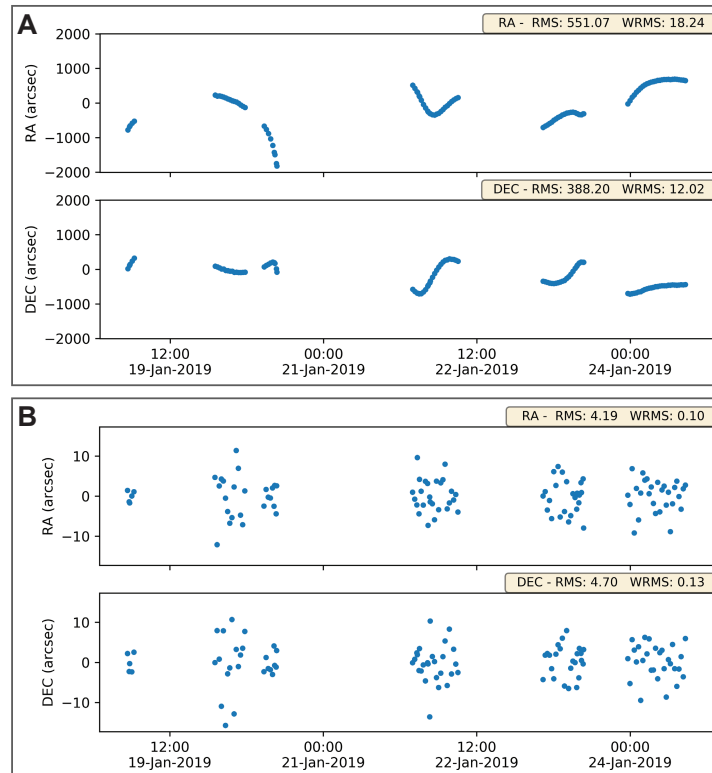


**Figure 23.** Postfit RA-DEC residuals for particle P1 when (A) neglecting the possibility of empirical accelerations and spacecraft position errors and (B) estimating these as a part of the fitting process.

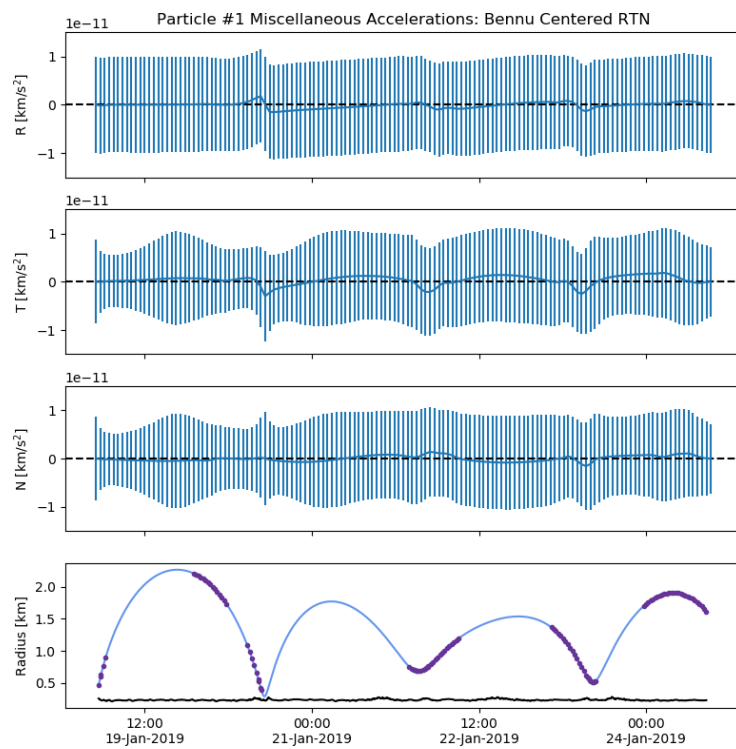


**Figure 24.** Empirical accelerations estimated for P1, projected into the Bennu-centered RTN frame. The bottom panel depicts the radii of the particle and sub-particle terrain during the observation arc. Observation times are marked by dots in the bottom panel.



1074 range of 10 to 20 cm. The estimated empirical accelerations are plotted in Fig. 24. In  
 1075 the figure, we observe that the estimated accelerations remain small, only a few times  
 1076  $10^{-12}$  km/s<sup>2</sup> and that the *a priori* constraint ( $10^{-11}$  km/s<sup>2</sup>) tends to dominate the *a*  
 1077 *posteriori* uncertainty. The position deviations due to such an acceleration are roughly  
 1078 a few meters per day, consistent with the deviations in the residuals seen in visible Fig. 23(a).  
 1079 Although none of the individual elements of the empirical acceleration history are sta-  
 1080 tistically significant, the ensemble effect is vital to obtaining a valid fit. There are surges  
 1081 in the empirical acceleration around the times of periapsis, which could be diagnostic  
 1082 of the source of the acceleration.

1083 We are unable to point to a definitive explanation for these empirical accelerations,  
 1084 which anyway need not have a single source. Given that there appear to be surges in the  
 1085 acceleration near periapsis, and that other objects show a periodic signal matching the  
 1086 orbital period, there is the possibility that mismodeling of gravity or Bennu radiation  
 1087 (reflected visible light or thermal emission) are contributors. But we also see accelera-  
 1088 tions far from periapsis. The fact that some anomalous accelerations are present at higher  
 1089 altitudes points to other sources of mismodeling. Our assumption of non-lambertian re-  
 1090 flected radiation is certainly suspect, as discussed by Dellagiustina et al. (2019). Or a  
 1091 slowly varying effective area-to-mass ratio, due to a precessing spin orientation, could  
 1092 cause a modulation in the effective SRP. However, both of these possibilities would man-  
 1093 ifest most strongly in the Sun direction, which we do not see in Sun-centered RTN pro-  
 1094 jections of the empirical accelerations. Despite the lack of clarity in the source of these  
 1095 accelerations, we do not so far see a compelling need to invoke mass loss, e.g., through  
 1096 outgassing or fission, as a likely cause of these accelerations.

## 1097 6 Summary and Conclusions

1098 In this report we present a catalog of trajectories and related analyses for 313 par-  
 1099 ticles seen in Bennu’s environment. About 2/3 of particles were on suborbital trajecto-  
 1100 ries, 1/7 departed on direct escape trajectories and 1/5 orbited Bennu for more than one  
 1101 complete revolution. We derived the sizes of the particles based on estimated area-to-  
 1102 mass ratios, combined with the photometric analyses presented by Hergenrother et al.  
 1103 (2019 in review, this collection). The results reveal a population of flake-like particles  
 1104 with median axis ratio 0.27 and equivalent diameters ranging from 0.22–6.1 cm, with me-  
 1105 dian 0.74 cm.

1106 The present results are not final as there are still more data to be processed, and  
 1107 future mission phases may yield new particle detections. Furthermore, even among the  
 1108 current data we will be revisiting failed and discarded solutions to obtain the correct so-  
 1109 lution whenever possible. Monte Carlo analysis of all impacts and ejections may yield  
 1110 additional cases of ejection caused by particle impacts, as well as new and expanded sets  
 1111 of particles associated by concurrent ejection events. Additional links likely remain to  
 1112 be found, and several apparently related particles have yet to be definitively connected.

1113 Selection effects are sure to have affected the particle catalog that we have devel-  
 1114 oped. Fast-moving particles leave the scene too rapidly to allow a suitable data set to  
 1115 be collected. Similarly, very slow ejections are aloft too short of a time to afford a suf-  
 1116 ficient number of detections. And small particles are below the detection threshold of  
 1117 the camera. Thus our catalog is predominantly composed of particles that are large enough  
 1118 ( $\gtrsim 2$  mm) and remain within a few kilometers of Bennu for at least a few hours. Addi-  
 1119 tionally, the imaging cadence for particle detections has been highly variable across the  
 1120 various OSIRIS-REx mission phases, which raises challenges in discerning if the level of  
 1121 Bennu activity depends on heliocentric distance. Future work may allow better insight  
 1122 into the debiased particle population and activity levels.

1123 We identified several ejection events with multiple simultaneous ejections emerg-  
1124 ing from the same location. While some of these events have been previously reported,  
1125 others are new, and we made no use of external information in identifying the particles  
1126 associated with the links. Given that we did not make presumptions or enforce constraints  
1127 on the ejection circumstances for the individual particle fits, the fact that we found 10  
1128 events comprising 40 particles altogether is a reassuring argument that our trajectories  
1129 are generally reliable.

1130 We also identified a case where a particle ricocheted from the surface, demonstrat-  
1131 ing that not all ejections are related to surface processes. The post-bounce orbit is at  
1132 substantially lower inclination and eccentricity, which should be typical of other simi-  
1133 lar events, suggesting that bouncing particles are likely to eventually re-impact in the  
1134 equatorial region. This may provide a pathway to understanding the overall role of par-  
1135 ticle ejections and associated mass movement on Bennu's surface, which likely has a con-  
1136 nection to the global shaping process pointed to by Scheeres et al. (2019) in relation to  
1137 the Roche lobe of Bennu. This discovery also allowed us to compute a coefficient of resti-  
1138 tution, which has implications for the mechanical properties of the boulders on Bennu's  
1139 surface, as well as that of the particles.

1140 Taking a subset of well-observed particles, we derived a Bennu gravity field com-  
1141 posed of spherical harmonics having clear signal through degree 8 and revealing density  
1142 inhomogeneities through degree 3. We await companion results from spacecraft track-  
1143 ing, which will serve as a vital validation of these results, and which can be combined  
1144 to yield a definitive gravity field.

1145 Despite striving for a complete and high-fidelity force model for our particle tra-  
1146 jectory propagation, we found it necessary to apply estimated empirical forces in order  
1147 to allow the computed particles trajectories to follow the observed paths. These empir-  
1148 ical accelerations often have a periodic signal matching the orbit period, suggesting mis-  
1149 modeling of one or more Bennu-related forces, e.g., emitted or reflected radiation from  
1150 Bennu onto the particle. We consider gravity mismodeling as an unlikely explanation  
1151 because even for an individual particle fit where the gravity was allowed to correct the  
1152 inconsistencies, the postfit residuals could not be reduced to acceptable levels. Particles  
1153 that repeatedly entered Bennu's shadow appear to show a stronger orbit periodic sig-  
1154 nal, at least in a few cases, pointing to the possibility that our eclipse model is some-  
1155 how deficient. And there remains the possibility that non-lambertian scattering and shape-  
1156 specific effects on reflected radiation pressure are important.

1157 Thus, while including these accelerations is vital to fit quality and trajectory ac-  
1158 curacy, we cannot point to a definitive source of the acceleration. Though mass loss due  
1159 to fission or outgassing cannot be ruled out, there is no compelling argument that these  
1160 processes must be acting on the particles. More intriguing in this regard are the several  
1161 apparently related particles that are following extraordinarily similar orbits, even approach-  
1162 ing to within a few meters at relative velocities  $<1$  mm/s, but for which a linked tra-  
1163 jectory solution is elusive. This is in stark contrast to the ease with which most linked  
1164 orbits fall into place. This could be a manifestation of an impulsive trajectory correc-  
1165 tion, as would be expected for the fission of a small grain from a larger and rapidly spin-  
1166 ning particle. A more complete understanding of these cases is left as future work.

1167 The results reported here have implications for the underlying cause of the ejec-  
1168 tions. Our findings generally agree with the predictions of Molaro et al. (2019 in review,  
1169 this collection) regarding fatigue fracturing due to the diurnal thermal cycle, in particu-  
1170 lar in regards to the size distribution of the fractured particles, assuming our distribu-  
1171 tion of particle axis ratios. The prevalence of ejections in the evening and afternoon is  
1172 also in accord, though our reduced number of ejections at polar latitudes does not match  
1173 the thermal fracturing models. On the other hand, the meteoroid impact hypothesis pro-  
1174 posed by Bottke et al. (2019 in review, this collection) makes predictions that are also

1175 consistent with our results. In particular, they predict most ejections will be on the af-  
 1176 ternoon/evening hemisphere, with an enhancement in the equatorial regions, which agrees  
 1177 well with our findings. The observation of over a hundred particles being simultaneously  
 1178 released in ejection events (Lauretta et al., 2019) seems to point more towards the me-  
 1179 teoroid hypothesis, though catastrophic releases of internal thermal stresses are known  
 1180 to occur in terrestrial settings. Neither of these hypotheses predict the significant num-  
 1181 ber of ejections seen from the opposite (morning) hemisphere, which could be a man-  
 1182 ifestation of ejections spawned by low-velocity particle impacts, either through ricochet-  
 1183 ing or lofting of different particles.

1184 There is certainly no reason to insist that a single mechanism drives the particle  
 1185 ejection phenomenon. The notion that thermal fracturing is grinding the surface into  
 1186 particles that can later be lofted by meteoroid bombardment is one way that these mech-  
 1187 anisms can be working in concert. This idea is particularly attractive given that our par-  
 1188 ticle sizes are an excellent match to those for thermal fracturing, while the latitudinal  
 1189 distribution of ejections is a better match to the meteoroid impact prediction. When com-  
 1190 bined with a background of ejections that are spawned by particle impacts, we have a  
 1191 cohesive story that meets our observational constraints. There may also be a superpo-  
 1192 sition of thermally driven ejections in addition to those arising from meteoroid impacts.  
 1193 Indeed, the mass loss mechanism seen on Phaethon at its perihelion (Li & Jewitt, 2013)  
 1194 could be taking place at Bennu, though at a dramatically reduced rate due to the higher  
 1195 heliocentric distance. Comparison of more refined ejection location information with high-  
 1196 resolution imagery may shed further light on this question.

1197 An important question is how prevalent the particle ejection phenomenon is across  
 1198 the near-Earth asteroid population, and even in the main asteroid belt. Given the re-  
 1199 port from Granvik et al. (2016) that only the small and dark asteroids are being cata-  
 1200 strophically disrupted at small heliocentric distances, the question looms large as to whether  
 1201 the phenomenon represented by Bennu’s particles is primarily associated with C-complex  
 1202 asteroids. At Bennu, the particles were discovered with an extraordinarily wide field-of-  
 1203 view instrument operated in a novel way so that the primary target was heavily over-  
 1204 exposed. This type of instrumentation and mode of operation has not been deployed in  
 1205 previous asteroid missions, but the discovery of particles around Bennu may motivate  
 1206 similar observations at other asteroids in the future.

## 1207 **Appendix A Average cross section of a tumbling spheroid**

We consider a tumbling ellipsoid with semiaxes  $a$ ,  $a$ ,  $b$ , defined by the equation

$$x^2/a^2 + y^2/a^2 + z^2/b^2 = 1.$$

In the body-fixed frame, we indicate the direction from the center of the ellipsoid to the Sun as  $\hat{\mathbf{u}} = (\cos \alpha \cos \delta, \sin \alpha \cos \delta, \sin \delta)$ . The cross-section of the ellipsoid visible from the Sun is given by the projection of the ellipsoid on the plane normal to  $\hat{\mathbf{u}}$ , which is defined by the directions  $\hat{\mathbf{v}} = (-\sin \alpha, \cos \alpha, 0)$  and  $\hat{\mathbf{w}} = (-\cos \alpha \sin \delta, -\sin \alpha \sin \delta, \cos \delta)$ . Given the corresponding coordinate system  $(u, w)$ , the projected ellipse is

$$u^2/a^2 + w^2/(a^2 \sin^2 \delta + b^2 \cos^2 \delta) = 1$$

1208 and therefore the area of the cross section is  $A = \pi a \sqrt{a^2 \sin^2 \delta + b^2 \cos^2 \delta}$ .

1209 We assume that, because of the tumbling rotation state, the body-fixed  $z$ -axis is  
 1210 uniformly distributed in space over time. This assumption is equivalent to having a uni-  
 1211 form distribution of  $\hat{\mathbf{u}}$  in the body-fixed frame. Therefore, the average cross-section can  
 1212 be computed as

$$\bar{A} = \frac{1}{2} \int_{-1}^1 A d(\sin \delta) = \frac{\pi a^2}{2} \int_{-1}^1 \sqrt{\sin^2 \delta + p^2 \cos^2 \delta} d(\sin \delta) = \pi a^2 f(p)$$

1213 where  $p = b/a$ . The definite integral can be evaluated to obtain

$$f(p) = \begin{cases} \frac{\sqrt{1-p^2+p^2} \operatorname{arcsinh}(\sqrt{1-p^2}/p)}{2\sqrt{1-p^2}} & p < 1 \\ 1 & p = 1 \\ \frac{\sqrt{p^2-1+p^2} \operatorname{arcsin}(\sqrt{p^2-1}/p)}{2\sqrt{p^2-1}} & p > 1 \end{cases} .$$

## 1214 Acknowledgments

1215 This material is based upon work supported by NASA under Contract NNM10AA11C  
1216 issued through the New Frontiers Program. This research was conducted in part at the  
1217 Jet Propulsion Laboratory, California Institute of Technology, under a contract with the  
1218 National Aeronautics and Space Administration. BR acknowledges funding support from  
1219 the Royal Astronomical Society (RAS) and the UK Science and Technologies Facilities  
1220 Council (STFC). The work of DV was partially funded by the Czech Science Founda-  
1221 tion (grant 18-06083S).

1222 Special thanks to B. Semenov and the Navigation and Ancillary Information Fa-  
1223 cility (NAIF) team at JPL, who provided crucial support in our effort to fit the parti-  
1224 cle detections and analyze the associated results. We are grateful to H. Roper for her  
1225 assistance in preparing the figures, and we thank M. Daly and M. Al Asad for sharing  
1226 the off-Bennu OLA detections. Finally, we thank the entire OSIRIS-REx Team for mak-  
1227 ing the encounter with Bennu possible.

1228 NavCam 1 images are or will be available via the TAGCAMS bundle in the Plan-  
1229 etary Data System  
1230 (<https://sbn.psi.edu/pds/resource/orex/tagcams.html>) (Bos et al., 2019). Observational  
1231 and derived data used in this work are available from Chesley et al. (2019). Our orbit  
1232 estimation software is derived from MIRAGE, now called MONTE, which is available  
1233 by license from <https://montepy.jpl.nasa.gov>. Our trajectory estimation relies on clas-  
1234 sical orbit determination algorithms as previously implemented by Brozović and Jacob-  
1235 son (2017). We also made use of the SPICE software suite using kernels publicly avail-  
1236 able on the NAIF website  
1237 (<https://naif.jpl.nasa.gov/naif/index.html>). The reduction and processing of angular po-  
1238 sition measurements is covered by Murray (1983), the propagation of trajectories and  
1239 treatment of time is described by, among others Moyer (2003), and the estimation ap-  
1240 proach that we use is that of Bierman (1977). All parameters needed to reproduce our  
1241 results are described in the text. The raw numbers for all figures in the text area can  
1242 be obtained from Chesley et al. (2019).

1243 ©2019.

## 1244 References

- 1245 Barnouin, O. S., Daly, M. G., Palmer, E. E., Gaskell, R. W., Weirich, J. R., John-  
1246 son, C. L., ... Osiris-Rex Team (2019, Mar). Shape of (101955) Bennu  
1247 indicative of a rubble pile with internal stiffness. *Nature Geoscience*, 12(4),  
1248 247-252. doi: 10.1038/s41561-019-0330-x
- 1249 Bierman, G. J. (1977). *Factorization Methods for Discrete Sequential Estimation*.  
1250 Academic Press.
- 1251 Borderies, N., & Longaretti, P.-Y. (1990, Mar). A New Treatment of the Albedo  
1252 Radiation Pressure in the Case of a Uniform Albedo and of a Spherical Satel-  
1253 lite. *Celestial Mechanics and Dynamical Astronomy*, 49(1), 69-98. doi:  
1254 10.1007/BF00048582

- 1255 Bos, B., Jackman, C., & Lauretta, D. (2019). *Origins, Spectral Interpretation,*  
 1256 *Resource Identification, Security, Regolith Explorer (OSIRIS-REx): Touch-and-*  
 1257 *Go Camera Suite (TAGCAMS) Bundle*, *urn:nasa:pds:orex.tagcams*. NASA  
 1258 Planetary Data System.
- 1259 Bos, B. J., Nelson, D. S., Pelgrift, J. Y., Liounis, A. J., Doelling, D., Norman,  
 1260 C. D., ... Lauretta, D. S. (2020, in press). In-Flight Calibration and Per-  
 1261 formance of the OSIRIS-REx Touch And Go Camera System (TAGCAMS).  
 1262 *Space Sci. Rev.*
- 1263 Bos, B. J., Ravine, M. A., Caplinger, M., Schaffner, J. A., Ladewig, J. V., Olds,  
 1264 R. D., ... Lauretta, D. S. (2018, Feb). Touch And Go Camera System (TAG-  
 1265 CAMS) for the OSIRIS-REx Asteroid Sample Return Mission. *Space Sci. Rev.*,  
 1266 *214*(1), 37. doi: 10.1007/s11214-017-0465-2
- 1267 Bottke, J., William F., Vokrouhlický, D., Rubincam, D. P., & Nesvorný, D. (2006,  
 1268 May). The Yarkovsky and Yorp Effects: Implications for Asteroid Dynam-  
 1269 ics. *Annual Review of Earth and Planetary Sciences*, *34*, 157-191. doi:  
 1270 10.1146/annurev.earth.34.031405.125154
- 1271 Bottke, W. F., Moorhead, A., Hergenrother, C. W., Michel, P., Schwartz, S.,  
 1272 Vokrouhlický, D., ... Lauretta, D. S. (2019 in review, this collection). Me-  
 1273 teoroid Impacts as a Source of Bennu's Particle Ejection Events. *JGR-Planets*.  
 1274 (Manuscript 2019JE006282)
- 1275 Brozović, M., & Jacobson, R. A. (2017, mar). The Orbits of Jupiter's Irregular  
 1276 Satellites. *The Astronomical Journal*, *153*(4), 147. doi: 10.3847/1538-3881/  
 1277 aa5e4d
- 1278 Capaccioni, F., Cerroni, P., Coradini, M., Farinella, P., Flamini, E., Martelli, G.,  
 1279 ... Zappala, V. (1984, Apr). Shapes of asteroids compared with fragments  
 1280 from hypervelocity impact experiments. *Nature*, *308*(5962), 832-834. doi:  
 1281 10.1038/308832a0
- 1282 Chesley, S., Hergenrother, C., Adam, C. D., Alkiew, K., Balram-Knutson, S.,  
 1283 Becker, K., ... Lauretta, D. (2019). *Supplementary Data for Bennu Par-*  
 1284 *ticle Analysis*. figshare.com. (Available during review at private URL  
 1285 <https://figshare.com/s/19e444f5f6fc9793c919>) doi: 10.6084/m9.figshare  
 1286 .11328398
- 1287 Clark, B. E., Binzel, R. P., Howell, E. S., Cloutis, E. A., Ockert-Bell, M., Chris-  
 1288 tensen, P., ... Mueller, M. (2011, Dec). Asteroid (101955) 1999 RQ36: Spec-  
 1289 troscopy from 0.4 to 2.4  $\mu\text{m}$  and meteorite analogs. *Icarus*, *216*(2), 462-475.  
 1290 doi: 10.1016/j.icarus.2011.08.021
- 1291 Collins, B. D., Stock, G. M., Eppes, M.-C., Lewis, S. W., Corbett, S. C., & Smith,  
 1292 J. B. (2018, Feb). Thermal influences on spontaneous rock dome exfoliation.  
 1293 *Nature Communications*, *9*, 762. doi: 10.1038/s41467-017-02728-1
- 1294 Daly, M. G., Barnouin, O. S., Dickinson, C., Seabrook, J., Johnson, C. L., Cunning-  
 1295 ham, G., ... Lauretta, D. S. (2017, Oct). The OSIRIS-REx Laser Altimeter  
 1296 (OLA) Investigation and Instrument. *Space Sci. Rev.*, *212*(1-2), 899-924. doi:  
 1297 10.1007/s11214-017-0375-3
- 1298 Dankowicz, H. (1994, April). Some special orbits in the two-body problem with ra-  
 1299 diation pressure. *Celestial Mechanics and Dynamical Astronomy*, *58*, 353-370.  
 1300 doi: 10.1007/BF00692010
- 1301 Dankowicz, H. (1995, March). The two-body problem with radiation pressure in a  
 1302 rotating reference frame. *Celestial Mechanics and Dynamical Astronomy*, *61*,  
 1303 287-313. doi: 10.1007/BF00051898
- 1304 Delbo, M., Libourel, G., Wilkerson, J., Murdoch, N., Michel, P., Ramesh, K. T., ...  
 1305 Marchi, S. (2014, Apr). Thermal fatigue as the origin of regolith on small  
 1306 asteroids. *Nature*, *508*(7495), 233-236. doi: 10.1038/nature13153
- 1307 Dellagiustina, D. N., Emery, J. P., Golish, D. R., Rozitis, B., Bennett, C. A., Burke,  
 1308 K. N., ... Osiris-Rex Team (2019, Mar). Properties of rubble-pile asteroid  
 1309 (101955) Bennu from OSIRIS-REx imaging and thermal analysis. *Nature*

- 1310 *Astronomy*, 3, 341-351. doi: 10.1038/s41550-019-0731-1
- 1311 Denneau, L., Jedicke, R., Grav, T., Granvik, M., Kubica, J., Milani, A., ... Scotti,  
1312 J. V. (2013, Apr). The Pan-STARRS Moving Object Processing System.  
1313 *PASP*, 125(926), 357. doi: 10.1086/670337
- 1314 Fröhlich, C., & London, J. (1986). *Revised Instruction Manual on Radiation Instru-*  
1315 *ments and Measurements* (Tech. Rep. No. WMO/TD-No. 149). World Climate  
1316 Research Programme, WMO/ICSU Joint Scientific Committee.
- 1317 Granvik, M., Morbidelli, A., Jedicke, R., Bolin, B., Bottke, W. F., Beshore, E., ...  
1318 Michel, P. (2016, Feb). Super-catastrophic disruption of asteroids at small  
1319 perihelion distances. *Nature*, 530(7590), 303-306. doi: 10.1038/nature16934
- 1320 Hamilton, V. E., Simon, A. A., Christensen, P. R., Reuter, D. C., Clark, B. E.,  
1321 Barucci, M. A., ... Osiris-Rex Team (2019, Mar). Evidence for widespread  
1322 hydrated minerals on asteroid (101955) Bennu. *Nature Astronomy*, 3, 332-340.  
1323 doi: 10.1038/s41550-019-0722-2
- 1324 Hartzell, C., Zimmerman, M., Hergenrother, C. W., & Lauretta, D. S. (2019 in re-  
1325 view, this collection). An evaluation of electrostatic lofting as an active mecha-  
1326 nism on Bennu. *JGR-Planets*. (Manuscript number 2019JE006228)
- 1327 Hergenrother, C. W., Maleszewski, C., Li, J.-Y., Pajola, M., Chesley, S. R., French,  
1328 A. S., ... Lauretta, D. S. (2019 in review, this collection). Photometry of  
1329 particles ejected from active asteroid (101955) Bennu. *JGR-Planets*.
- 1330 Hergenrother, C. W., Maleszewski, C. K., Nolan, M. C., Li, J. Y., Drouet  
1331 D'Aubigny, C. Y., Shelly, F. C., ... OSIRIS-REx Team (2019, Mar). The  
1332 operational environment and rotational acceleration of asteroid (101955)  
1333 Bennu from OSIRIS-REx observations. *Nature Communications*, 10, 1291.  
1334 doi: 10.1038/s41467-019-09213-x
- 1335 Hsieh, H. H., & Jewitt, D. (2006, Apr). A Population of Comets in the Main Aster-  
1336 oid Belt. *Science*, 312(5773), 561-563. doi: 10.1126/science.1125150
- 1337 Jekeli, C. (1983). A numerical study of the divergence of spherical harmonic series  
1338 of the gravity and height anomalies at the earth's surface. *Bulletin géodésique*,  
1339 57(1), 10-28. Retrieved from <https://doi.org/10.1007/BF02520909> doi: 10  
1340 .1007/BF02520909
- 1341 Jewitt, D., Agarwal, J., Weaver, H., Mutchler, M., & Larson, S. (2013, Nov). The  
1342 Extraordinary Multi-tailed Main-belt Comet P/2013 P5. *ApJ*, 778(1), L21.  
1343 doi: 10.1088/2041-8205/778/1/L21
- 1344 Jewitt, D., Hsieh, H., & Agarwal, J. (2015). The Active Asteroids. In P. Michel,  
1345 F. DeMeo, & W. F. Bottke (Eds.), *Asteroids IV* (pp. 509-531). Tucson: Univ.  
1346 Arizona Press.
- 1347 Lauretta, D. S., Hergenrother, C. W., Chesley, S. R., Leonard, J. M., Pelgrift, J. Y.,  
1348 Adam, C. D., ... Wolner, C. W. V. (2019). Episodes of particle ejection from  
1349 the surface of the active asteroid (101955) Bennu. *Science*, 366(6470). doi:  
1350 10.1126/science.aay3544
- 1351 Leonard, J. M., Adam, C. D., Pelgrift, J. Y., Lessac-Chenen, E. J., Nelson, D. S.,  
1352 Antreasian, P. G., ... Lauretta, D. S. (2019 in review, this collection). Initial  
1353 Orbit Determination and Event Reconstruction from Estimation of Particle  
1354 Trajectories about (101955) Bennu. *Earth and Space Science*. (Manuscript  
1355 2019EA000937)
- 1356 Li, J., & Jewitt, D. (2013, Jun). Recurrent Perihelion Activity in (3200) Phaethon.  
1357 *AJ*, 145(6), 154. doi: 10.1088/0004-6256/145/6/154
- 1358 Liounis, A. J., Small, J. L., Swenson, J. C., Lyzhoft, J. R., Ashman, B. W., Get-  
1359 zandanner1, K. M., ... Lauretta, D. S. (2019 in review, this collection).  
1360 Autonomous Detection of Particles and Tracks in Optical Images. *Earth and*  
1361 *Space Science*. (Manuscript number 2019EA000843)
- 1362 McMahan, J. W., Scheeres, D. J., Chesley, S. R., French, A., Brack, D., Farnocchia,  
1363 D., ... Lauretta, D. S. (2019 in review, this collection). The Dynamics of  
1364 Ejected Particles Around Bennu. *JGR-Planets*. (Manuscript 2019JE006229)

- 1365 McMahon, J. W., Scheeres, D. J., Hesar, S. G., Farnocchia, D., Chesley, S., & Lau-  
 1366 retta, D. (2018, Feb). The OSIRIS-REx Radio Science Experiment at Bennu.  
 1367 *Space Sci. Rev.*, *214*(1), 43. doi: 10.1007/s11214-018-0480-y
- 1368 Michikami, T., Hagermann, A., Kadokawa, T., Yoshida, A., Shimada, A., Hasegawa,  
 1369 S., & Tsuchiyama, A. (2016, Jan). Fragment shapes in impact experiments  
 1370 ranging from cratering to catastrophic disruption. *Icarus*, *264*, 316-330. doi:  
 1371 10.1016/j.icarus.2015.09.038
- 1372 Mignard, F., & Henon, M. (1984). About an unsuspected integrable problem. *Celes-*  
 1373 *tial mechanics*, *33*(3), 239-250.
- 1374 Milani, A., La Spina, A., Sansaturio, M. E., & Chesley, S. R. (2000, Mar). The As-  
 1375 teroid Identification Problem. III. Proposing Identifications. *Icarus*, *144*(1), 39-  
 1376 53. doi: 10.1006/icar.1999.6261
- 1377 Milani, A., Sansaturio, M. E., & Chesley, S. R. (2001, Jun). The Asteroid Identifica-  
 1378 tion Problem IV: Attributions. *Icarus*, *151*(2), 150-159. doi: 10.1006/icar.2001  
 1379 .6594
- 1380 Molaro, J. L., Hergenrother, C. W., Chesley, S. R., Hanna, R. D., Haberle, C. W.,  
 1381 Ballouz, R.-L., ... Lauretta, D. S. (2019 in review, this collection). Thermal  
 1382 fatigue as a driving mechanism for activity on asteroid Bennu. *JGR-Planets*.  
 1383 (Manuscript 2019JE006325.)
- 1384 Moyer, T. D. (2003). *Formulation for Observed and Computed Values of Deep Space*  
 1385 *Network Data Types for Navigation*. Wiley.
- 1386 Murray, C. A. (1983). *Vectorial Astrometry*. CRC Press.
- 1387 Park, R. S., Konopliv, A. S., Bills, B. G., Rambaux, N., Castillo-Rogez, J. C., Ray-  
 1388 mond, C. A., ... Preusker, F. (2016, Sep). A partially differentiated interior  
 1389 for (1) Ceres deduced from its gravity field and shape. *Nature*, *537*(7621),  
 1390 515-517. doi: 10.1038/nature18955
- 1391 Pelgrift, J. Y., Lessac-Chenen, E. J., Adam, C. D., Leonard, J. M., Nelson, D. S.,  
 1392 McCarthy, L., ... Lauretta, D. S. (2019 in review, this collection). Reconstruc-  
 1393 tion of Bennu Particle Events from Sparse Data. *Earth and Space Science*.  
 1394 (Manuscript 2019EA000938)
- 1395 Reimond, S., & Baur, O. (2016, Mar). Spheroidal and ellipsoidal harmonic expan-  
 1396 sions of the gravitational potential of small Solar System bodies. Case study:  
 1397 Comet 67P/Churyumov-Gerasimenko. *Journal of Geophysical Research (Plan-*  
 1398 *ets)*, *121*(3), 497-515. doi: 10.1002/2015JE004965
- 1399 Richter, K., & Keller, H. U. (1995). On the stability of dust particle orbits around  
 1400 cometary nuclei. *Icarus*, *114*(2), 355-371.
- 1401 Rieger, S. M., Scheeres, D. J., & Barbee, B. (2019, May). Orbital Stability Re-  
 1402 gions for Hypothetical Natural Satellites of (101955) Bennu. *Journal of Space-*  
 1403 *craft and Rockets*, *56*(3), 789-800. doi: 10.2514/1.A34160
- 1404 Rosengren, A. J., & Scheeres, D. J. (2014, Mar). On the Milankovitch orbital ele-  
 1405 ments for perturbed Keplerian motion. *Celestial Mechanics and Dynamical As-*  
 1406 *tronomy*, *118*(3), 197-220. doi: 10.1007/s10569-013-9530-7
- 1407 Rozitis, B., Emery, J. P., Siegler, M. A., Susorney, H. C. M., Molaro, J. L., Hergen-  
 1408 rother, C. W., & Lauretta, D. S. (2019 in review, this collection). Implications  
 1409 for ice stability and particle ejection from high-resolution temperature model-  
 1410 ing of asteroid (101955) Bennu. *JGR-Planets*. (manuscript 2019JE006323)
- 1411 Rozitis, B., & Green, S. F. (2011, Aug). Directional characteristics of thermal-  
 1412 infrared beaming from atmosphereless planetary surfaces - a new thermophys-  
 1413 ical model. *MNRAS*, *415*(3), 2042-2062. doi: 10.1111/j.1365-2966.2011.18718  
 1414 .x
- 1415 Rozitis, B., & Green, S. F. (2012, Jun). The influence of rough surface thermal-  
 1416 infrared beaming on the Yarkovsky and YORP effects. *MNRAS*, *423*(1), 367-  
 1417 388. doi: 10.1111/j.1365-2966.2012.20882.x
- 1418 Rozitis, B., & Green, S. F. (2013, Jul). The influence of global self-heating on the  
 1419 Yarkovsky and YORP effects. *MNRAS*, *433*(1), 603-621. doi: 10.1093/mnras/

- 1420 stt750  
1421 Sánchez, P., & Scheeres, D. J. (2014, May). The strength of regolith and rubble pile  
1422 asteroids. *Meteoritics and Planetary Science*, *49*(5), 788-811. doi: 10.1111/  
1423 maps.12293  
1424 Scheeres, D. J. (1999). Satellite Dynamics about small bodies: Averaged Solar Radi-  
1425 ation Pressure Effects. *The Journal of the Astronautical Sciences*, *47*, 25-46.  
1426 Scheeres, D. J. (2012a). *Orbital Motion in Strongly Perturbed Environments: Appli-*  
1427 *cations to Asteroid, Comet and Planetary Satellite Orbiters*. Springer-Praxis,  
1428 London (UK).  
1429 Scheeres, D. J. (2012b). Orbit Mechanics about Asteroids and Comets. *Journal of*  
1430 *Guidance, Control and Dynamics*, *35*(3), 987-997.  
1431 Scheeres, D. J., Britt, D., Carry, B., & Holsapple, K. A. (2015). Asteroid Interi-  
1432 ors and Morphology. In *Asteroids iv* (p. 745-766). doi: 10.2458/azu.uapress  
1433 \_9780816532131-ch038  
1434 Scheeres, D. J., & Marzari, F. (2002). Spacecraft dynamics far from a comet. *The*  
1435 *Journal of the Astronautical Sciences*, *50*(1), 35-52.  
1436 Scheeres, D. J., McMahon, J. W., French, A. S., Brack, D. N., Chesley, S. R.,  
1437 Farnocchia, D., . . . Osiris-Rex Team (2019, Mar). The dynamic geophys-  
1438 ical environment of (101955) Bennu based on OSIRIS-REx measurements.  
1439 *Nature Astronomy*, *3*, 352-361. doi: 10.1038/s41550-019-0721-3  
1440 Tapley, B. D., Schutz, B. E., & Born, G. H. (2004). *Statistical orbit determination*.  
1441 Burlington: Academic Press. doi: [https://doi.org/10.1016/B978-012683630-1/](https://doi.org/10.1016/B978-012683630-1/50025-4)  
1442 [50025-4](https://doi.org/10.1016/B978-012683630-1/50025-4)  
1443 Vokrouhlický, D. (1998, Jul). Diurnal Yarkovsky effect as a source of mobility of  
1444 meter-sized asteroidal fragments. I. Linear theory. *A&A*, *335*, 1093-1100.  
1445 Vokrouhlický, D., Bottke, W. F., Chesley, S. R., Scheeres, D. J., & Statler, T. S.  
1446 (2015). The Yarkovsky and YORP effects. In P. Michel, F. DeMeo, &  
1447 W. F. Bottke (Eds.), *Asteroids IV* (pp. 509-531). Tucson: Univ. Arizona  
1448 Press.  
1449 Werner, R. A. (1997, Dec). Spherical harmonic coefficients for the potential of a  
1450 constant-density polyhedron. *Computers and Geosciences*, *23*(10), 1071-1077.  
1451 doi: 10.1016/S0098-3004(97)00110-6  
1452 Werner, R. A., & Scheeres, D. J. (1996, Sep 01). Exterior gravitation of a polyhe-  
1453 dron derived and compared with harmonic and mascon gravitation representa-  
1454 tions of asteroid 4769 castalia. *Celestial Mechanics and Dynamical Astronomy*,  
1455 *65*(3), 313-344. Retrieved from <https://doi.org/10.1007/BF00053511> doi:  
1456 10.1007/BF00053511